

AD-A178 176

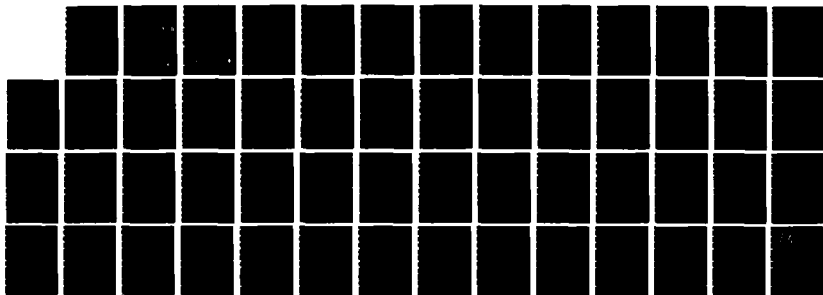
LASER MATERIALS FOR THE 067 MICROMETERS TO 25  
MICROMETERS RANGE(U) RCA LABS PRINCETON NJ  
M TODA ET AL. MAR 87 RCA-PRRL-86-CR-4 NASA-CR-4050

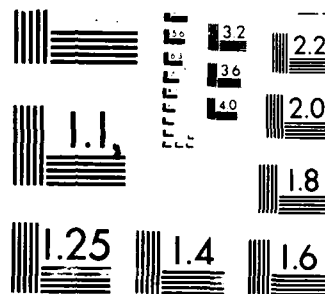
1/1

UNCLASSIFIED

F/G 20/5

NL





MICROCOPY RESOLUTION TEST CHART  
NATIONAL BUREAU OF STANDARDS-1963-A

AD-A178 176

NASA Contractor Report 4050  
HDL-CR-86-351-1

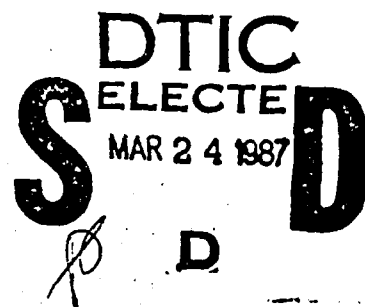
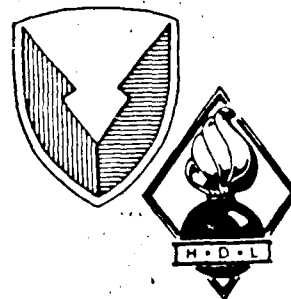
Laser Materials for the  
0.67- $\mu$ m to 2.5- $\mu$ m Range

Minoru Toda, Thomas J. Zamerowski,  
Ivan Ladany, and Ramon U. Martinelli

CONTRACT NAS1-17351  
MARCH 1987

**DISTRIBUTION STATEMENT A**  
Approved for public release  
Distribution Unlimited

**NASA**



2

NASA Contractor Report 4050  
HDL-CR-86-351-1

## Laser Materials for the 0.67- $\mu\text{m}$ to 2.5- $\mu\text{m}$ Range

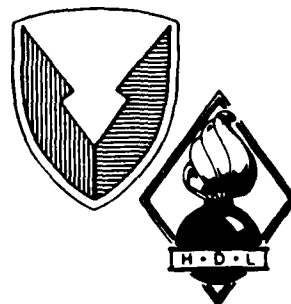
Minoru Toda, Thomas J. Zamerowski,  
Ivan Ladany, and Ramon U. Martinelli

*RCA Laboratories  
Princeton, New Jersey*

Prepared for  
Langley Research Center  
under Contract NAS1-17351  
and  
U.S. Army Laboratory Command  
Harry Diamond Laboratories

**NASA**  
National Aeronautics  
and Space Administration  
Scientific and Technical  
Information Branch

1987



U.S. Army Laboratory Command  
**Harry Diamond Laboratories**  
Adelphi, MD 20783-1197

# PREFACE

This assessment study report covers work performed at RCA Laboratories from 23 September 1985 to 18 June 1986 under Contract No. NAS1-17351 by the Optoelectronics Research Laboratory, B. Hershenov, Director. The Group Head was M. Ettenberg and the Project Scientist was I. Ladany. Staff members and support personnel in addition to the authors who contributed to this work, and the area of their contributions, were:

- \*R. E. Enstrom--vapor phase epitaxy
- D. B. Gilbert--measurements
- M. G. Harvey--device assembly
- \*P. A. Longeway--detectors
- E. De Piano--device fabrication
- T. Tarangioli--device fabrication
- J. T. Andrews--device fabrication

Accession For	
NTIS CRA&I	<input checked="" type="checkbox"/>
DTIC TAB	<input type="checkbox"/>
Unannounced	<input type="checkbox"/>
Justification	
By	
Distribution/	
Availability Codes	
Dist	Avail and/or Special
A-1	



\*Member technical staff

## TABLE OF CONTENTS

Section	Page
PREFACE .....	1
1. INTRODUCTION .....	9
2. STRUCTURE OF HIGH POWER PULSE LASERS .....	10
2.1 Double Heterostructure .....	10
2.2 Lateral Structure Definition .....	12
2.3 Improvement of Pulse Power Output .....	13
3. MATERIAL SELECTION AND SUITABLE COMBINATIONS .....	14
4. PROPOSED LASER STRUCTURES .....	18
4.1 0.67- $\mu$ m Wavelength Region .....	18
4.2 1.44- $\mu$ m Wavelength Region .....	26
4.3 1.93- and 2.5- $\mu$ m Wavelength Regions .....	29
5. DETECTORS .....	40
5.1 0.67- $\mu$ m Devices .....	41
5.2 1.44- $\mu$ m Devices .....	43
5.3 1.93- and 2.5- $\mu$ m Devices .....	43
6. CONCLUSIONS .....	46
REFERENCES .....	47
APPENDIX A. THEORETICAL BACKGROUND OF SASAKI EQUATIONS .....	55

# LIST OF ILLUSTRATIONS

Figure		Page
1.	Energy band diagram of a double heterojunction .....	11
2.	Cross sectional view of an oxide stripe laser with double heterostructure .....	13
3.	Variations of energy gap and band structure with respect to composition for III-V mixed semiconductors .....	16
4.	Variations in relative dielectric constants with respect to composition for III-V mixed semiconductors .....	16
5.	Relationship between energy bandgap and relative dielectric constants .....	17
6.	Energy bandgap diagram of InGaAlP and constant diagram of InGaAlP .....	20
7.	Energy bandgap diagrams for InGaAsP and AlGaAsP .....	22
8.	Energy bandgap for InGaAsP .....	24
9.	Potential well and electron wavelength energy states for electrons and holes in a quantum well .....	26
10.	Threshold current density at 300 K as a function of lasing wavelength for AlGaAs laser diodes .....	27
11.	Double-barrel vapor phase growth reactor .....	28
12.	Output power vs pulse current of a typical 1.44- $\mu$ m laser developed under contract .....	30
13.	Emission spectrum of a typical 1.44- $\mu$ m laser developed under contract .....	30
14.	Energy bandgap diagram for AlGaAsSb .....	32
15.	Energy bandgap diagram for InGaAsSb and dielectric constant diagram for InGaAsSb .....	33
16.	Energy bandgap diagram for InAsSbP .....	35
17.	Output power vs bandgap of InAsSbP on InAs .....	36
18.	Energy bandgap diagram of InAlGaAs .....	37
19.	Energy bandgap diagram of InGaAsP .....	38
20.	Structure of PIN photodetector .....	40
21.	Quantum efficiency of various photodetectors using different materials .....	41

# LIST OF ILLUSTRATIONS (continued)

Figure	Page
22. Structure of PIN photodetector using InGaAs heterojunction of RCA product .....	44
23. Proposed structure of PIN photodetector using InGaAs on graded substrate .....	45



## 1. INTRODUCTION

This assessment study report summarizes the available information dealing with semiconductor lasers capable of operating at 0.67-, 1.44-, 1.93-, and 2.5- $\mu\text{m}$  wavelengths and then presents recommendations as to the most promising system for each wavelength. A major assumption is that the lasers will operate at room temperature in the pulsed mode at a relatively low duty cycle and with high output power.

Unfortunately, most published results describe devices that do not have the exact desired wavelengths. Therefore, this report deals primarily with the possibility of modifying the described device material compositions to meet specifications. In addition, some totally new compositions are proposed.

The first experimental demonstrations of semiconductor lasers were prepared with GaAs p-n junctions in 1962. They operated in the pulsed mode at 77 K [1-3]. Since then, a lot of effort has gone into achieving room temperature cw operation. It was found that a double heterojunction (DH) was necessary to reduce the threshold current. Furthermore, lateral confinement of the active lasing region into a narrow width stripe has become a common technique [4,5]. Although the subject devices do not have to operate in the cw mode, the DH and a stripe geometry are necessary for higher output power, reduced current drive, beam definition, and operating life.

A great deal of effort has also been applied towards extending laser operating life and improving reliability. The reliability of DH lasers was improved remarkably with the development of techniques that remove mechanical strain, provide passivation, exclude oxygen from the growth atmosphere, improve ohmic contacts, and control crystalline degradation and catastrophic facet damage [6-13]. Even though the subject devices do not require very long life, all the techniques mentioned above improve the maximum power output limit.

A number of papers have been written on lasers that operate near the required wavelengths. For the short wavelengths ( $\sim 0.67 \mu\text{m}$ ), there is need for a very sharply focused beam for high density optical information storage, such as audio or video disc players and optical printers [14]. This need arises because the focussed area becomes smaller for the shorter wavelengths, thus yielding higher energy density and higher resolution. Therefore, short wavelength lasers are actively being investigated and very encouraging laboratory experiments have been reported.

The intermediate region of 1.44  $\mu\text{m}$  is close to the 1.3- and 1.55- $\mu\text{m}$  ranges where present optical fiber communication systems are being developed for optical fibers with low transmission loss (0.47 dB/km) and zero dispersion at  $\lambda = 1.3 \mu\text{m}$  and even lower loss (0.2 dB/km) at  $\lambda = 1.55 \mu\text{m}$  [14-17]. The InGaAsP/InP lasers for communication purposes are very well developed, and control of the wavelength by changing the material composition is very well established [14]. Therefore, InGaAsP can be selected for 1.44- $\mu\text{m}$  wavelength devices with great confidence of success.

For the 1.93- to 2.5- $\mu\text{m}$  range, there are attempts to develop longer wavelength lasers for communication purposes because of Rayleigh scattering, the intrinsic loss mechanism due to non-uniformities in the refractive index which decreases with a factor of  $\lambda^{-4}$ . In present quartz fibers, however, the signal above 1.7  $\mu\text{m}$  is strongly attenuated due to the molecular vibration of Si, O, and (OH). Consequently, there is a search for new fiber materials [14] to replace quartz, and lasers in this wavelength will no doubt become important in the future.

There is also a need for longer wavelength sources in spectrometry, or photometry, to analyze gaseous molecules whose characteristic absorptions are in the 1- to  $\sim 10\text{-}\mu\text{m}$  range. However, commercial demands in both the gaseous analysis and fiber communication field are not large now, and research in the longer wavelength region is not very active.

## 2. STRUCTURE OF HIGH POWER PULSE LASERS

### 2.1. Double Heterostructure

The energy band structure of an efficient high power laser (Fig. 1) should contain a double heterojunction [17]. The active layer, in which light amplification takes place, is sandwiched between two cladding layers that have higher energy bandgaps than the active layer; one cladding layer is doped p-type and the other n-type. When a forward bias voltage is applied to the junction, electrons are injected from the n-type cladding layer into the active layer and holes are injected from the p-type cladding into the active layer.

Since the p-type cladding is a large energy wall for injected electrons, it blocks the flow of electrons while the n-type cladding layer blocks the flow of holes. In this way, electron-hole recombination is limited to the active

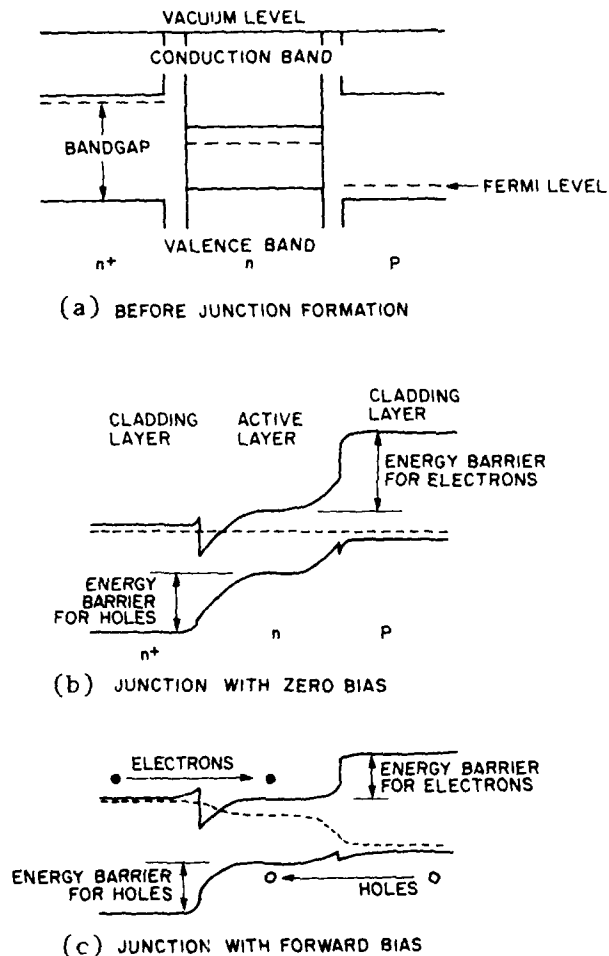


Figure 1. Energy band diagram of a double heterojunction: (a) Before high bandgap  $n^+$ , low bandgap  $n$ , and high bandgap  $p$  materials are combined; (b) After junction is formed, the sharp notch and step may be smoothed out by interdiffusion of atoms or melting each other. Fermi level comes on a common line at zero bias condition; (c) At a forward bias condition, electrons and holes are injected into the active region and blocked by the energy wall.

region. The refractive index of the active layer must be higher than that of the cladding layer, so that the active layer can function as an optical waveguide in trapping the radiation. Thus, the quantum efficiency of a DH laser is very high and this structure has to be a prime choice for efficient high power lasers.

The difference in the bandgaps of active and cladding layers should be more than ten times the thermal energy,  $kT \approx 26 \text{ meV}$  at  $T = 300 \text{ K}$ , because the

carrier is energized roughly up to the  $kT$  value and the energy walls have to block the higher energy carriers in the thermal distribution, even when the energy wall is reduced at forward bias conditions. If the energy wall is not high enough, some of the recombination takes place outside the active region. The resultant radiation has a different wavelength and cannot be guided into the active region. A high energy wall can be realized by choosing a higher energy bandgap material for the cladding layer, but the higher bandgap material does not necessarily have a lower refractive index (this is discussed in detail in Section 2.2).

Another requirement for the DH structure is the matching of the lattice constants for epitaxially grown active and cladding materials. When the lattice mismatch in the DH structure is appreciable, lattice defects grow rapidly to form dark lines or spot defects due to the heat generated by non-radiative recombination and residual stress [14,17]. However, lattice matching of the active or cladding material to the substrate material is not always necessary because of the use of a "graded scheme" in which the lattice constant gradually varies from that of the cladding material to that of the substrate through the insertion of a graded-composition intermediate layer.

## 2.2. Lateral Structure Definition

The DH discussions above deal with the compositional variations in the depth direction. This section considers structural variations in the plane parallel to the junction.

A number of studies have been devoted to methods for constraining lateral modes to obtain effective coupling into fiber cores. The lateral structure of the active region of suitable lasers is usually a stripe geometry, achieved by either gain guiding or index guiding.

The width of the stripe can be made narrow enough to obtain single mode operation, but the present high power pulse laser does not have to operate in a single mode. If the stripe width is large, i.e., 8 mils, multiple near-field spots are formed in the 8-mil-long facet region. An ideal lens set at its focal length (i.e., 1 inch) converts the radiation from lasing spots into parallel beams, but the beam has  $0.46^\circ$  lateral divergence, which means the beam spreads to an 8-foot-wide region at a 1000-foot distance. To reduce the horizontal

divergence of the beam coming out from an appropriate lens, the width of the stripe has to be reduced.

The simplest way of confining the active layer width is to use the oxide stripe geometry in which guiding action in the lateral direction is obtained by gain guiding produced by constricting the current region (Fig. 2).

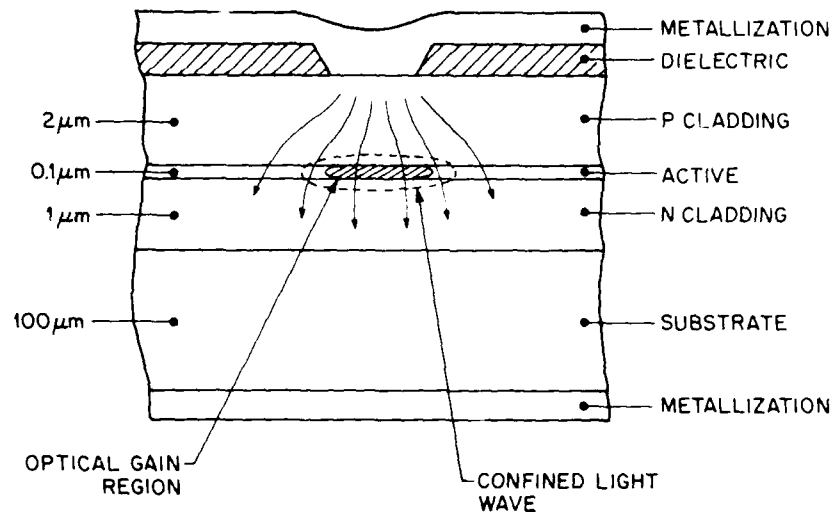


Figure 2. Cross-sectional view of an oxide stripe laser with double heterostructure. The light is guided in the high gain region of high current density.

### 2.3. Improvement of Pulse Power Output [14,17]

#### 2.3.1. Kinks

When the forward current is increased, the measured output does not necessarily increase. The output-current curve of gain-guided lasers sometimes shows an unstable change of the gradient, called a kink. This kink is associated with mode hopping, and it can be suppressed by reducing the stripe width to the point where only one mode can exist (typically less than 10  $\mu\text{m}$ ). It is also possible to have a wide gain-guided emitting region by properly phasing each emission and in essence making a phased array. However, mode hopping associated with wide-stripe lasers may not be objectionable in the present application.

#### 2.3.2. Larger Energy Wall to Suppress Carrier Leakage

For narrow stripe-width lasers, the output power can be seen to saturate at some high current level. At a large forward bias condition (Fig. 1a), the

energy wall of the DH structure is reduced [18-20]. Also, the concentration of high energy carriers increases due to the increased temperature or the hot electron effect at a high injection level [21]. The carrier heating effect becomes predominant when free carrier absorption or Auger recombination [22] is large at a high injection condition because the recombination energy cannot be radiated to the outside. Carrier leakage tends to occur in such a high temperature condition. The increase of threshold current with increasing temperature results in decreased optical gain. An effective solution to carrier leakage is increasing the height of the energy wall height.

### 2.3.3. Improvement of Facet Structure

At a high output power level, the facet degrades due to a photochemical reaction with water vapor or oxygen adsorption and also catastrophic damage. Passivation by  $\text{Al}_2\text{O}_3$  or  $\text{SiO}_2$  coating on the facet doubles the maximum power level to approximately 10 to 14  $\text{MW}/\text{cm}^2$  of 100-nsec pulses for GaAs/AlGaAs lasers[23]. To reduce absorption at the facet region, the bandgap at the facet region can be slightly enlarged by variations in impurity doping [24]. In this case, a maximum output of 10 to 20  $\text{MW}/\text{cm}^2$  for 100 nsec pulses was observed, which is 1.5 to 1.8 W for a 10- $\mu\text{m}$ -wide stripe.

## 3. MATERIAL SELECTION AND SUITABLE COMBINATIONS

As described earlier, the necessary conditions for material combinations for double heterostructures are

- (1) a suitable bandgap combination, which means the active region has a lower bandgap with direct transitions,
- (2) a suitable refractive index combination, which means the active region has a higher index, and
- (3) lattice constants of the active and cladding layers that agree and match those of the substrate directly or gradually.

To select materials from combinations of commonly used III-V elements--In, Ga, Al, As, Sb, and P--A. Sasaki et al [25] compiled two charts (Fig. 3 and 4). One shows the direct and indirect energy bandgaps and the lattice constant; the other presents the relative dielectric constant. These two charts include all the combinations of the often-used III-V elements. Figure 3

shows the bandgap by curved solid lines for direct transition and by curved dotted lines for phonon-assisted indirect transition. The straight lines show that any point on the line has the same lattice constant as that of a corner binary material, which is often used for the substrate. All the arbitrary equal-lattice-constant lines are parallel in a material region. A point inside a square or triangle area is expressed by a certain ratio of the mixture of binary materials. The basic concept, equations and parameters used for drawing these curves are given in Appendix A.

The relative dielectric constant,  $\epsilon_r$ , which is directly related to the refractive index  $n$  through  $n \cong \sqrt{\epsilon_r}$ , is given in Fig. 4.

The material for the active region should be chosen from the specified wavelength  $\lambda$  using the relationship

$$E_g(\text{eV}) = 1.2399/\lambda (\mu\text{m}) .$$

Therefore, suitable bandgaps are 1.85 eV ( $\lambda = 0.67 \mu\text{m}$ ), 0.86 eV ( $\lambda = 1.44 \mu\text{m}$ ), 0.64 eV ( $\lambda = 1.93 \mu\text{m}$ ), 0.496 eV ( $\lambda = 2.5 \mu\text{m}$ ). With Fig. 3, the composition of each active layer material can be determined from a point showing the necessary bandgap value on an equal lattice constant line drawn from a corner where there is a name of a binary material.

For example, for active layer material that emits 1- $\mu\text{m}$  wavelength radiation, find a line of 1.24 eV that starts from a little below InP--which is on the uppermost horizontal line--and extends in the left-down direction, passing near the GaAs point and further down near the GaSb point. Also, another branch starts as above, but proceeds to the right in the downward direction and ends a little above the other InP point at the bottom central region. The line encompasses five square regions and two triangle regions. Thus, seven different material regions are chosen. (Actually, three more square regions and two triangle regions, including a 1.24-eV line, are found in the right-hand side regions, but the discussion is similar.)

The substrate material whose lattice constant matches the material to be grown can be found as follows. The left part of the 1.24-eV line intersects with a straight line starting from InP in the GaP-InP-GaAs-InAs square region (InGaAsP) and also intersects in the GaP-GaAs-GaSb triangle region (GaAsSbP). The right part of the 1.24-eV line intersects with three parallel straight lines starting from InAs, GaSb, and AsSb in both the InAlAsSb and InAlSbP square

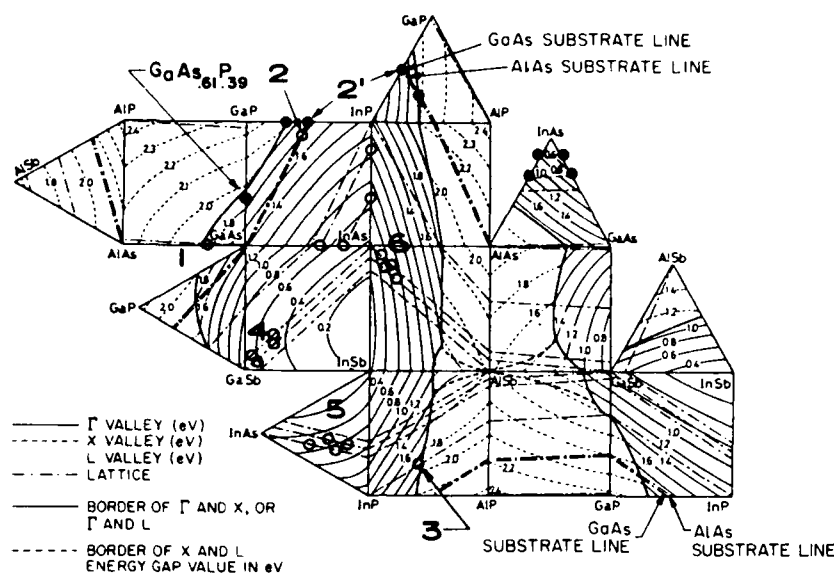


Figure 3. Variations of energy gap and band structure with respect to composition for III-V mixed semiconductors. Thin solid, broken, and dotted lines denote equi-energy gaps of  $\Gamma$ , X, and L valleys, respectively. Thus, the band structure in the region of thin solid lines is direct. The thick solid line is the borderline between  $\Gamma$  and X or  $\Gamma$  and L valleys, and the thick broken line is the borderline between X and L valleys. The thin dash-and-dot line is an equilattice-constant line. The numerical values indicate energy gaps in eV.

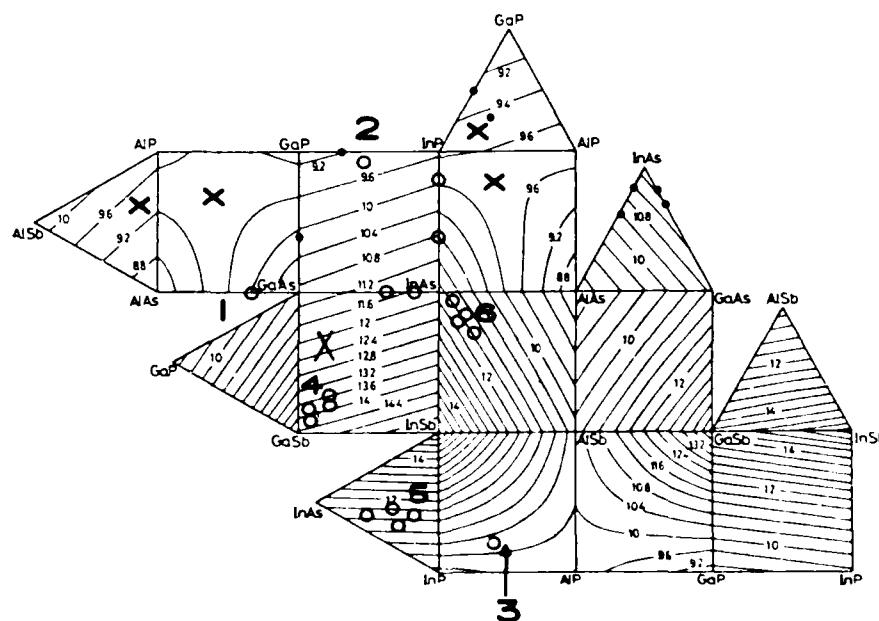


Figure 4. Variations in relative dielectric constants with respect to composition for III-V mixed semiconductors.



regions. A point at the intersection gives the material composition of the active layer and also specifies the substrate to be used.

The cladding layer materials are chosen from compositions that yield a bandgap step more than 10 times the thermal energy  $kT$  ( $\cong 26$  meV at room temperature) and are on the same lattice constant line as that of the active layer. The refractive index for the cladding material has to be lower than that of the active layer; this has to be checked in Fig. 4.

The cladding materials for the famous GaAs/AlGaAs and InGaAsP/InP lasers fortunately have higher bandgaps and smaller indices. This higher bandgap lower index tendency is observed in a very rough version in various binaries (Fig. 5), although the plots of  $\epsilon_r$  vs  $E_g$  for the binaries are pretty much dispersed. As for ternaries and quaternaries, if the equal bandgap lines in Fig. 3 were exactly parallel to the equal dielectric constant lines in Fig. 4, the high bandgap and low index tendency would hold exactly.

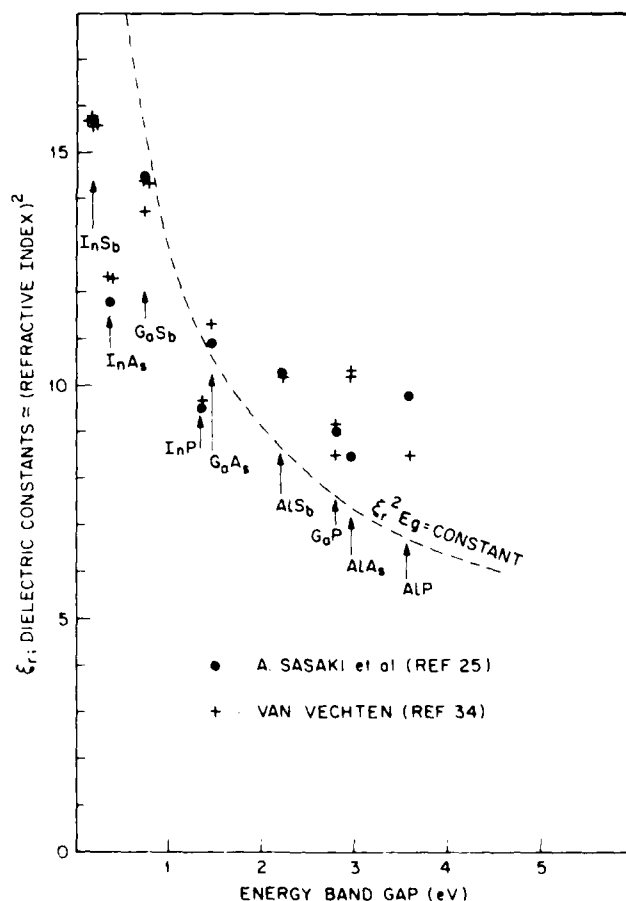


Figure 5. Relationship between energy bandgap and relative dielectric constants.

The line shape or gradient is totally different for AlAsSbP, AlGaAsP, InGaAlP, InAlAsP, InGaAsSb regions marked by x in Fig. 4. This should be noted for selection of new material combinations.

Actually, most researchers discuss the bandgap for DH structures, but not the refractive index, and some published articles proposed laser structures with the wrong combination, while some textbooks and review papers give the incorrect impression that a lower refractive index is always caused by a higher bandgap [14,17].

The reason for this belief is the concept, called Moss' rule [26], which says energy level separations are inversely proportional to the square of the dielectric constant, so that the threshold wavelength of the absorption edge or  $E_g$  would be given by the approximate relation [27]

$$n^4 E_g = \text{constant}.$$

Moss' concept, however, is only a rough rule. Actual values for III-V binary materials do not lie only on a smooth curve. There are several cases with higher bandgap materials having higher refractive indexes as seen in Fig. 5. The agreement between the constant  $n^4 E_g$  curve and real values is not very good.

#### 4. PROPOSED LASER STRUCTURES

##### 4.1. 0.67- $\mu$ m Wavelength Region

In this section, we apply the concepts discussed above to obtain detailed recommendations concerning suitable materials for the desired wavelengths.

The 0.67- $\mu$ m wavelength corresponds to the bandgap of 1.85 eV. First, 1.85-eV lines have to be found in Fig. 3, and then intercepts located on the substrate line starting from available binary substrates. These points are numbered 1, 2, 3 in Figs. 3 and 4. The material compositions are (1)  $\text{Al}_{0.35}\text{Ga}_{0.55}\text{As}_{0.98}\text{P}_{0.02}$ , (2)  $\text{In}_{0.46}\text{Ga}_{0.54}\text{P}_{0.95}\text{As}_{0.05}$  for GaAs substrates, and (3)  $\text{In}_{0.6}\text{Al}_{0.4}\text{Sb}_{0.24}\text{P}_{0.76}$  for InP substrates. The lasing wavelength is slightly longer than the designed value because the temperature rise at a high injection level tends to reduce the bandgap. Therefore, slightly larger energy lines, such as 1.9 eV, have to be considered.

The material (1) has a very small amount of P and belongs to the AlGaAs category, about which a number of reports are available. The material (2) was also reported for short wavelength devices. The material (3) was not found in the literature. This material should be excluded because the point is close to the indirect transition boundary, and the materials on the substrate line from InP show higher dielectric constant for higher band gap regions as seen in Figs. 3 and 4.

There are other intercept points between 1.85-eV (or 1.9-eV) lines and AlAs or GaAs substrate lines. The materials on AlAs lines should be excluded from investigation because AlAs is deliquescent. The GaAs line and the 1.9-eV line intercept at the point 2' on the side of the uppermost triangle region formed by GaP, InP, AlP points, and this material ( $\text{Ga}_{0.5}\text{In}_{0.5}\text{P}$ ) is discussed in the following section. Also, the 1.9-eV line and the GaAs line intercept at another point on the side of the right-bottom-corner-square region formed by InSb, GaSb, GaP, InP. The cladding material on this GaAs line does not make a good DH structure because the bandgap difference is too small. This covers all the possible material combinations for a 0.67- $\mu\text{m}$  device, which will now be taken up in more detail.

#### 4.1.1. InGaP/InGaAlP on GaAs Substrate

The InGaAlP system is shown in the triangular areas located at the uppermost regions in Figs. 3 and 4. Only the pertinent regions are enlarged and shown in Fig. 6(a) and (b). The GaAs substrate line covers the range from 1.91 to 2.15 eV in the direct transition region whose material composition is  $\text{In}_{0.5}(\text{Ga}_{1-x}\text{Al}_x)_{0.5}\text{P}$  with  $0 < x < 0.47$ . The range of  $0.47 < x < 1$  is in the indirect transition region with 2.15 to 2.26 eV.

Even though the lowest bandgap on the GaAs line (point 2') is a little higher than the specified bandgap of 1.85 eV, the actually observed wavelength is 0.68 to 0.69  $\mu\text{m}$  [28-31] for  $\text{In}_{0.5}\text{Ga}_{0.5}\text{P}$  due to the heating of the active layer. This longer wavelength can be tuned to 0.67  $\mu\text{m}$  by adding a small amount of Al into the active and cladding materials. The shortest wavelength laser with  $\lambda = 0.626 \mu\text{m}$  is observed when  $x = 0.17$  [30]. However, this active-cladding material combination does not seem to provide the right optical guide structure, since higher bandgap material with a higher Al concentration has a higher refractive index, as seen in Fig. 6(b).

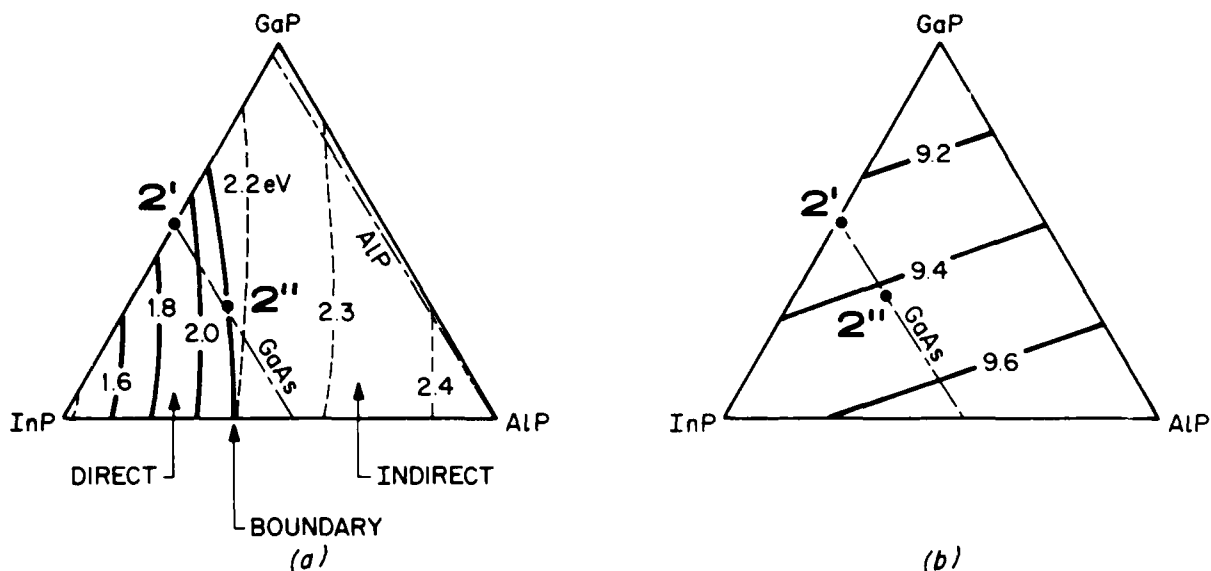


Figure 6. (a) Energy bandgap diagram of InGaAlP. The point 2' is active and 2'' is cladding material, and (b) Dielectric constant diagram of InGaAlP

Nevertheless, very good results were reported recently by K. Kobayashi et al [31]. They describe room-temperature cw operation of  $\text{In}_{0.5}\text{Ga}_{0.5}\text{P}/(\text{Al}_{0.4}\text{Ga}_{0.6})_{0.5}\text{In}_{0.5}\text{P}$  laser (points 2' and 2'' in Fig. 6), with a very low threshold current of  $4.1 \text{ kA/cm}^2$ ,  $\lambda = 0.69 \mu\text{m}$  [31]. The characteristic temperature  $T_0$  is 90 K, which means the temperature dependence of  $J_{\text{th}}$  is better than that of the commercially available InGaAsP/InP laser, but worse than that of the GaAs/AlGaAs lasers. The details on growth conditions have been reported by the same group [32,33]. These very good results are inconsistent with the use of the wrong refractive index guide structure, and thus require further discussion.

The higher dielectric constant of  $(\text{Al}_{0.4}\text{Ga}_{0.6})_{0.5}\text{In}_{0.5}\text{P}$  than of  $\text{In}_{0.5}\text{Ga}_{0.5}\text{P}$ , as seen in Fig. 6(b), originates from the higher dielectric constant of AlP with  $\epsilon_r = 9.78$  and the lower dielectric constant of GaP with  $\epsilon_r = 9.036$  in Table 1 by Sasaki et al. Other reports give different values [34], such as a minimum  $\epsilon_r$  value for AlP of 8.5 and a reported maximum  $\epsilon_r$  for GaP of 9.1. As for AlP, growth of the pure crystal is difficult because it is unstable in humid air, making the data unreliable. The numbers for the dielectric constants by various investigators are shown in Table 1. The values consistently agree for each material except for AlP and AlAs. Therefore, the triangle region of InGaAlP in Fig. 4 or the chart in Fig. 6(b) may not be reliable. The fact that very good laser properties were obtained suggests that the DH structure with higher refractive index of the active layer is correct. The value of AlAs does not affect the result of the discussions because the points are far from all the laser materials.

TABLE 1. DIELECTRIC CONSTANTS

Semi-conductor	Conduction valley			Lattice constant (Å)	Dielectric constant*	Dielectric Constant†
	Γ	X	L			
AlP	3.58	2.46	~3.6	5.4625	9.78	8.5 (a)
AlAs	2.95	2.16	2.93	5.6611	8.5	10.2 (b) 10.3 (a)
AlSb	2.20	1.63	1.63	6.1355	10.24	10.2 (c) 10.2 (d)
GaP	2.78	2.26	2.67	5.4495	9.036	9.1 (e) 9.1 (f) 8.5 (c) 8.5 (d)
GaAs	1.43	1.86	1.72	5.653	10.9	11.3 (f) 10.9 (c) 10.9 (d)
GaSb	0.721	1.02	0.821	6.094	14.44	13.7 (f) 14.4 (c) 14.4 (d)
InP	1.34	2.06	1.86	5.868	9.52	9.6 (c) 9.6 (d)
InAs	0.359	1.56	1.46	6.053	11.8	12.3 (c) 12.3 (d)
InSb	0.175	0.955	0.775	6.478	15.7	15.7 (c) 15.7 (d)

\*From A. Sasaki et al [18]

†From J. A. Van Vechten [34] Dielectric Constant  
Each number is from a different source(a) Value predicted on basis of trends noted  
in text; experimental data are not firm.

(b) S. K. Kurtz, private communication.

(c) E. Burstein, H. M. Brodsky, and G. Lucovsky  
Int. J. Quantum Chem., 1s, 759 (1967).(d) M. Hasa and B. W. Henvis, J. Phys. Chem.  
Solids, 23, 1099 (1962).(e) A. S. Barker, Phys. Rev., 165, 917 (1968).

(f) J. W. Allen, private communication.

#### 4.1.2. InGaAsP/AlGaAs(P) on GaAs

The InGaAsP system is shown by the central square region of the three uppermost square regions, and AlGaAsP is shown by the next left side square. These two square regions are enlarged and shown in Fig. 7. The composition of InGaAsP, whose lattice constant matches that of GaAs, is shown by the straight

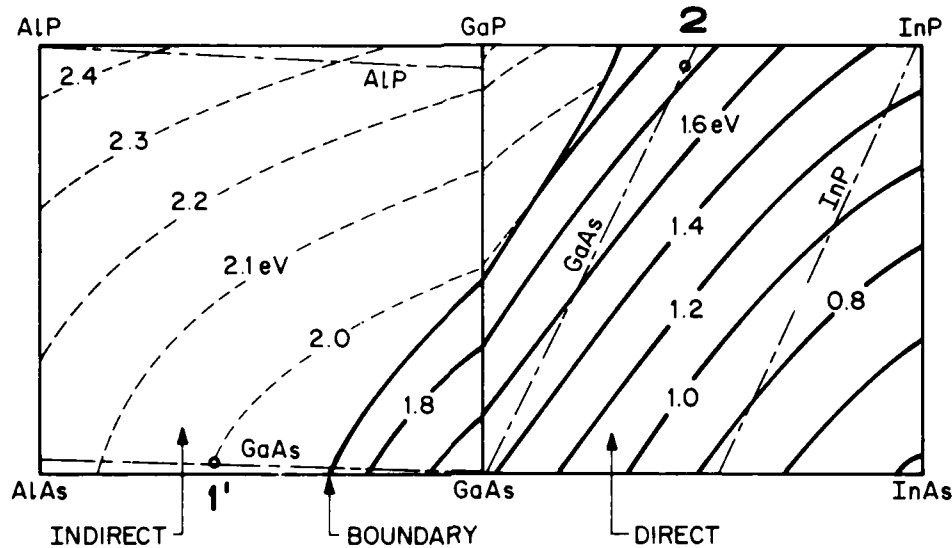


Figure 7. Energy bandgap diagrams for InGaAsP and AlGaAsP.

line starting from the corner of GaAs; the composition of 1.85 eV on the GaAs line is numbered by "2" in Fig. 7. Higher bandgap energy material for cladding cannot be chosen from the same material on the GaAs line because the bandgap becomes smaller towards GaAs along the line. One possibility is to use AlGaAs, which has been investigated in detail. To assure higher bandgap and lower index, the Al content  $x$  of  $\text{Al}_x\text{Ga}_{1-x}\text{As}$  has to be more than 0.6.

K. Kishino et al [35] reported on the  $\text{In}_{0.47}\text{Ga}_{0.53}\text{As}_{0.05}\text{P}_{0.95}/\text{Al}_{0.6}\text{Ga}_{0.4}\text{As}$  structure (points 2 and 1' in Fig. 7) with very encouraging results of a 30-mW output at room temperature, 100-ns pulse operation, and  $J_{\text{th}} = 8 \text{ kA/cm}^2$  at  $\lambda = 0.67 \mu\text{m}$ . The characteristic temperature,  $T_0$ , was 53 K. The width of the stripe was  $71 \mu\text{m}$  [35]. When the width was reduced to  $8 \mu\text{m}$ , cw operation up to 208 K was achieved, but  $J_{\text{th}}$  increased to 13 to  $25 \text{ kA/cm}^2$  because of the spreading of the current [36]. Another group [37] reported details of LPE growth, but the laser characteristics were not as good as those of Kishino et al.

#### 4.1.3. InGaAsP/InGaAsP on GaAs Substrate

As described in the previous section, the bandgap of InGaAsP lattice matched to GaAs ranges from 1.87 to 1.43 eV; cladding material for 1.85-eV active material cannot be provided by the same material with different composition. When a lower bandgap material (closer to GaAs) is used for the active layer, the wavelength becomes longer than 0.67  $\mu\text{m}$ . S. Mukai et al [38] reported on this example with 0.704- and 0.725- $\mu\text{m}$  wavelengths.

#### 4.1.4. InGaAsP/InGaAsP on Graded Lattice Constant GaAs<sub>0.6</sub>P<sub>0.4</sub> Layer Substrate

Commercial GaAs<sub>0.6</sub>P<sub>0.4</sub> substrates grown on GaAs are available for LED use. The lattice constant of GaAs<sub>0.6</sub>P<sub>0.4</sub> is different from that of GaAs so that an intermediate layer of GaAs<sub>x</sub>P<sub>1-x</sub> is inserted, with the x value changing from zero on the GaAs surface to 0.6 on the final growth surface. The chart for InGaAsP was extracted from Fig. 3 and enlarged for Fig. 8. The material compositions whose lattice constants match the GaAs<sub>0.6</sub>P<sub>0.4</sub> substrate are expressed by the straight line starting from the GaAs<sub>0.6</sub>P<sub>0.4</sub> point. The bandgap varies from 1.9 to 2.0 eV for direct transition and 2.0 to 2.14 eV for indirect transition. Therefore, the active material should be GaAs<sub>0.6</sub>P<sub>0.4</sub>, or close to this composition, and the cladding material should be found from a point with higher bandgap on the substrate line.

A fairly good result was reported by H. Kressel et al at RCA [39]. The output was 4.3 mW for cw operation at 10°C with  $J_{\text{th}} = 6.6 \text{ kA/cm}^2$  at a 0.68- $\mu\text{m}$  wavelength using GaAs<sub>0.7</sub>P<sub>0.3</sub> for the active material and In<sub>0.34</sub>Ga<sub>0.66</sub>P for the cladding (Fig. 8). The operating life was tested for a drive current 20% less than  $I_{\text{th}}$ , and the output decreased by 40% after 2000 hours of operation. This degradation is substantially larger than that of AlGaAs lasers emitting at about 0.8  $\mu\text{m}$ . The reason for the degradation was thought to be misfit dislocations propagating from the graded substrate, since so-called cross-hatched patterns were seen on all the grown surfaces of each step. Other researchers described the same surface pattern [38,40], and detailed crystal growth conditions were also investigated [41,42].

However, A. Usui et al [42] reported that very high crystalline quality In<sub>0.07</sub>Ga<sub>0.93</sub>As<sub>0.51</sub>P<sub>0.49</sub> for the active material and In<sub>0.32</sub>Ga<sub>0.68</sub>P for the cladding can be grown on graded GaAs<sub>0.61</sub>P<sub>0.39</sub> substrates when the growth

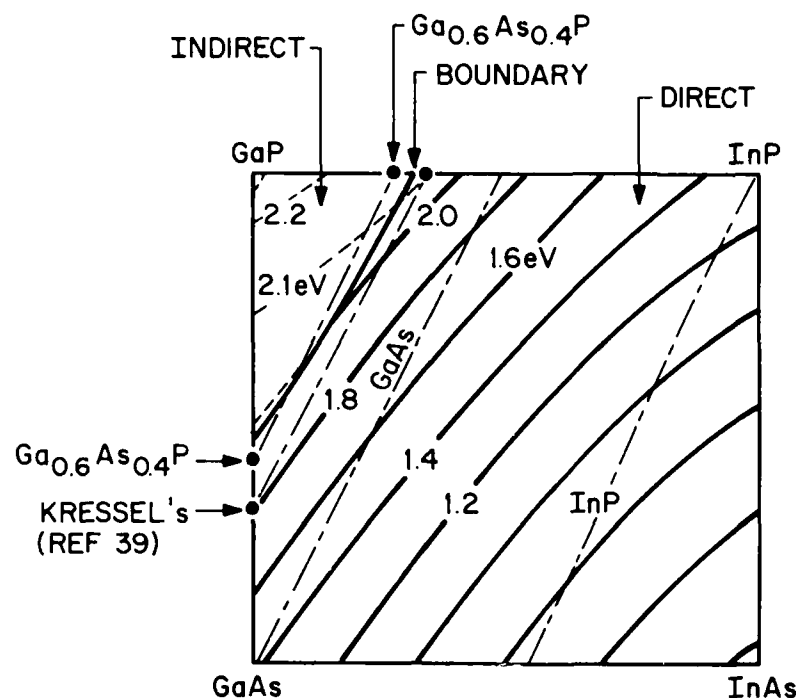


Figure 8. Energy bandgap for InGaAsP. The black points are short wavelength materials.

condition is chosen so as to introduce an intentional lattice mismatching of  $3 \times 10^{-3}$  between the grown layers and the graded substrate. The reason for the improvement was not fully understood but they suggested it was cancellation of strains between the newly introduced strain and the one in the substrate. The laser made under this growth condition showed a lower threshold current than Kressel's ( $5.6 \text{ kA/cm}^2$  at  $\lambda = 0.65 \mu\text{m}$ ), and degradation was not observed. The output power was not measured, but cw operation was possible up to  $-27^\circ\text{C}$  and room temperature pulse operation was obtained.

#### 4.1.5. AlGaAs/AlGaAs on GaAs Substrate

The most thoroughly investigated laser is  $\text{Al}_x\text{Ga}_{1-x}\text{As}$ , whose bandgap can be modified to around 1.85 eV. The bandgap increases with increasing  $x$  and  $E_g = 1.85 \text{ eV}$  at  $x = 0.35$ . However, there is a problem because the satellite band, which is the indirect transition band and is normally located above the direct transition band, comes closer and closer to the direct band with increasing  $x$  [14,17,43] so that more injected carriers undergo an indirect (nonradiative) transition.



This indirect transition leads to higher threshold currents with shorter wavelength. The best DH lasers grown by LPE [44], MOCVD [45], and MBE [46] show that the threshold current becomes 14 times higher at the 0.67- $\mu\text{m}$  composition compared to that of the long wavelength region [47]. Short life or degradation was also observed [43]. This is caused by internal stress due to the thermal expansion difference between the substrate and active layer, a heating problem aggravated in the cw condition. In pulse operation, heating should be much less severe, but the lowered output due to the indirect transition is not favorable.

#### 4.1.6. Multi-Quantum Well (MQW) Laser

The property of quantum wells is explained in various review papers [48,49]. The principle can be summarized as follows. According to quantum mechanics, an electron confined by a pair of potential barriers is not allowed to have continuous energy values but only discrete energies due to the interaction between the barrier distance and the energy-dependent electron wave, similar to standing wave phenomena.

When an electron or hole in a semiconductor is confined with a lower energy state in a very thin layer whose thickness is reduced to the order of the de Broglie wavelength, the same phenomenon of discrete energy levels appears for carrier momentum in the thickness direction (Fig. 9). Thus, the minimum energy of electrons and holes is raised to the lowest allowable level. The observed wavelength due to recombination in this thin layer is not necessarily much shorter than the one corresponding to the bandgap energy, because of longitudinal optical phonon-assisted transitions which make the wavelength longer. Actually, the wavelength is very close to, or slightly shorter than, that of the bandgap energy [48,50]. The most striking effects are the threshold current, which is decreased, and the power output which becomes larger.

T. Saku et al [47] have grown various lasers by molecular beam epitaxy (MBE) and observed threshold currents for lasing as a function of compositions  $x$  for  $\text{Al}_x\text{Ga}_{1-x}\text{As}$  MQW (six layers, 100 Å for each thickness) with a 300-Å thick  $\text{Al}_{0.5}\text{Ga}_{0.5}\text{As}$  separation layer. The observed wavelength varied from 0.728 to 0.651  $\mu\text{m}$  for the range of  $0.15 < x < 0.35$ . The conventional bandgap for this composition corresponds to 1.6 to 1.85 eV, and the corresponding wavelengths are 0.795 to 0.670  $\mu\text{m}$ . The actually observed wavelengths are 3 to 6% less than given by conventional bandgap energy.

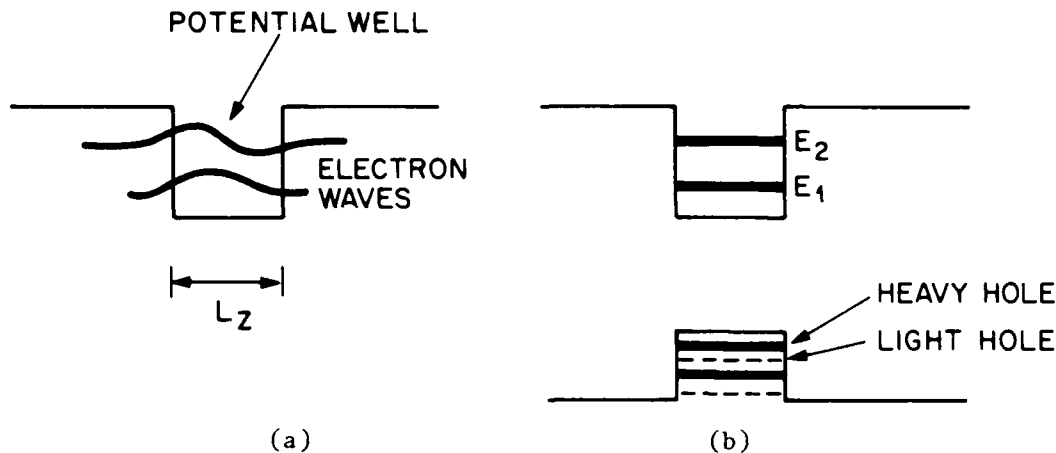


Figure 9. (a) Potential well and electron wavelength (de Broglie wavelength =  $h/p \approx L_z$ , where  $P$  is the momentum) and (b) Energy states for electrons and holes in a quantum well.

The threshold current density was almost constant for the range of the compositions to which the 0.728- to 0.665  $\mu\text{m}$  wavelength corresponds as seen in Fig. 10.

On the other hand, conventional MOCVD-grown DH lasers corresponding to this wavelength range were very different in that the threshold current increased very much with increasing Al content, and the threshold current at 0.67  $\mu\text{m}$  was more than one order of magnitude higher. The life or degradation of the AlGaAs MQW laser [47] was not discussed, but it is very likely that the reduced life problem of conventional DH lasers in the short wavelength region (0.67  $\mu\text{m}$ ) does not appear here because the small threshold current and high quantum efficiency of MQW lasers lead to less heating and less internal strain because of the thermal expansion difference between the lasing region and substrate.

Taking full advantage of the above-mentioned reduced heating, the use of a phase-locked multiple array structure (40 stripe array emitters in parallel) produced 2.5-W cw power at a 4-A drive current at room temperature [51,52].

#### 4.2. 1.44- $\mu\text{m}$ Wavelength Region

RCA has produced 1.3- and 1.55- $\mu\text{m}$  pulsed high-power lasers with a 500-mW output at a 2.0-A current level, 1- $\mu\text{s}$  pulse length, and 100-kHz repetition rate. These devices can be modified to the defined wavelength. Therefore, RCA decided to use technology based on the InGaAsP system. In these structures, InGaAsP is used as the active layer and InP as the cladding layer.

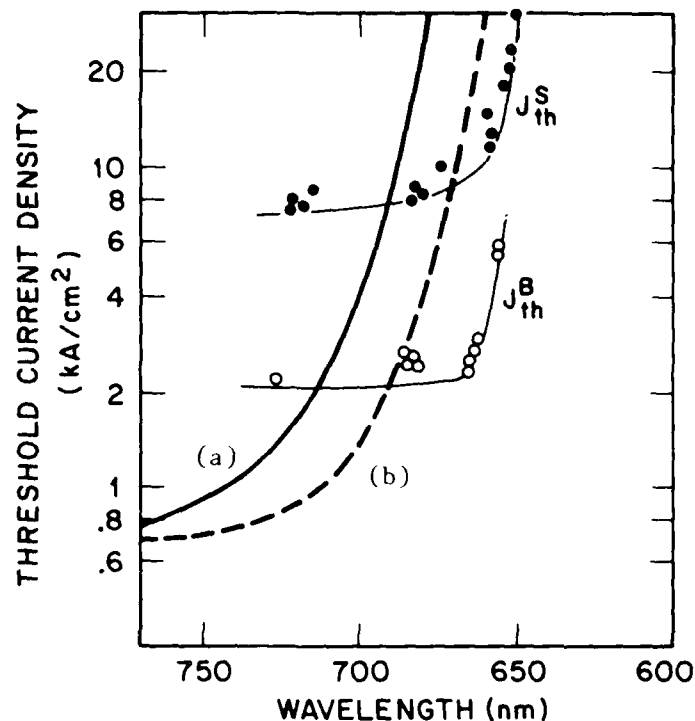


Figure 10. Threshold current density at 300 K as a function of lasing wavelength for AlGaAs laser diodes. Curve (a) is the lowest  $J_{th}$  realized so far by conventional DH laser diodes with  $Al_xGa_{1-x}As$  active layer. Curve (b) is the result of MO-CVD grown SQW laser with 40 to 60-nm QW layer. Present data are indicated by open and closed circles. Open circles ( $J_{th}^B$ );  $J_{th}$  for broad area diodes ( $80 \times 500 \mu m^2$ ). Closed circles ( $J_{th}^S$ );  $J_{th}$  for stripe geometry diodes ( $10 \times 200 \mu m^2$ ).

#### 4.2.1. Growth System

Lasers are grown in an RCA-developed double-barrel VPE reactor (Fig. 11), using group V hydride and group III metal chlorides. With this type of system, two independent gas compositions (InP and the quaternary compound) and their respective hydrogen carriers can be set up at the same time. The tubulations for the two different gas compositions are joined to a common growth chamber partitioned in half by a quartz plate to prevent the gases from mixing.

The substrate sits on a sample holder off axis from its positioning rod. By turning this rod to the left or to the right of the partition, the substrate is exposed to one or the other gas stream. Each gas stream can be independently doped. The thicknesses of the layers are measured by looking with a scanning

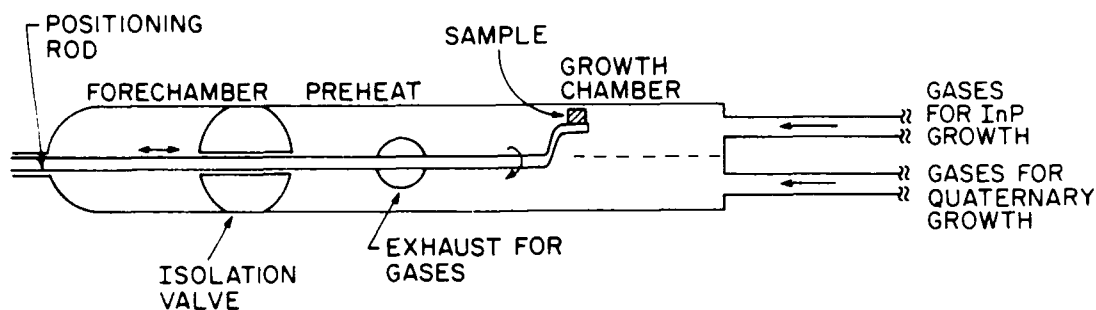


Figure 11. Double-barrel vapor phase growth reactor. Sample action can be switched to different gases region.

electron microscope (SEM) at the chemically stained edge of an angle-lapped surface. The profile of doping densities is measured by capacitance-voltage curves while chemical etching is being done. N-type doping is obtained from  $H_2S$  and p-type doping from zinc metal. Parameters obtained for the 1.44- $\mu m$  material are given in Table 2.

TABLE 2. THICKNESS AND DOPING DENSITY

Material	Thickness ( $\mu m$ )	Doping Density
$p^+$ -quaternary	$0.38 \pm -0.03$	$2.2 \times 10^{19} \text{ cm}^{-3} \text{ Zn}$
P-InP	$2.40 \pm -0.5$	$1.9 \times 10^{19} \text{ cm}^{-3} \text{ Zn}$
$n^-$ -quaternary	$0.175 \pm -0.005$	
n-InP	2 to 3	$1.1 \times 10^{18} \text{ cm}^{-3} \text{ S}$
$n^+$ -InP substrate	380	$0.6-1.0 \times 10^{18} \text{ cm}^{-3} \text{ S}$

#### 4.2.2. Growth Procedure

The epitaxial layers are deposited on an InP substrate that is cleaned and polish-etched just prior to growth. The substrate has had an etch pit density of less than  $10^3/\text{cm}^2$ , and is oriented to be  $2^\circ$  off the (100) plane in the  $\langle 110 \rangle$  direction.

The substrate is put into the forechamber of the reactor. After flushing with an inert gas, followed by hydrogen, the substrate is placed into the

preheat section of the reactor and brought up to the growth temperature in an atmosphere of phosphine. When the sample reaches the desired temperature (695°C), it is inserted into the InP portion of the growth tube and a buffer layer of n-InP is grown. The substrate is then switched to the other side, and an undoped layer of the 1.44- $\mu$ m quaternary is grown. The other two layers are grown in a similar fashion.

#### 4.2.3. Growth Analysis

The composition of the active layer is determined from the maximum in the photoluminescence (PL) spectrum. Its lattice constant is determined by X-ray diffraction after the top two layers are removed by etching. The PL peak position for the wafer used to fabricate the present lasers was 1.427  $\mu$ m, and the lattice constant mismatch relative to InP was 0.1%. This measurement yields a composition of  $\text{In}_{0.64}\text{Ga}_{0.36}\text{As}_{0.74}\text{P}_{0.26}$ .

For high power, the oxide stripe configuration appears to be advantageous, and, therefore, it was decided to use the same structure for this program.

The results achieved are demonstrated in Figs. 12 and 13, which show the pulsed output power and the pulsed spectrum obtained from typical devices.

There is some difficulty in measuring the power output under pulsed conditions. The Fig. 12 data are believed to be accurate to within 10% of the true value. The pulse length in these measurements was 400 ns.

The power was determined by first measuring the dc power using by a large-area Ge detector claimed by the manufacturer to be calibrated with traceability to the National Bureau of Standards. Next, the detector was biased in the reverse direction, and the same range of powers measured to correct for the different bias mode. Then, the device was operated with 400-ns pulses, and the measurements were repeated at low power and carried forward to high powers. At the higher powers, neutral density filters were used in the light path in order to avoid overdriving the detector; the attenuation of these filters was determined in independent tests at the present wavelength.

#### 4.3. 1.93- and 2.5- $\mu$ m Wavelength Regions

The 1.93- and 2.5- $\mu$ m wavelengths correspond to 0.64- and 0.496-eV bandgaps, which are present in three regions of the charts. One is the upper central

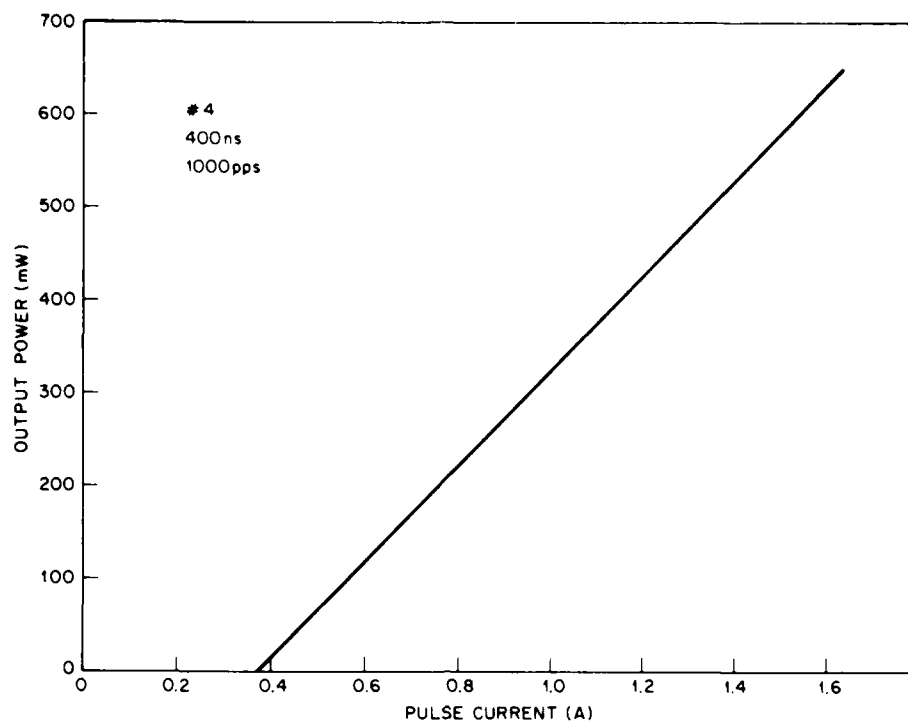


Figure 12. Output power vs pulse current of a typical 1.44-μm laser developed under contract.

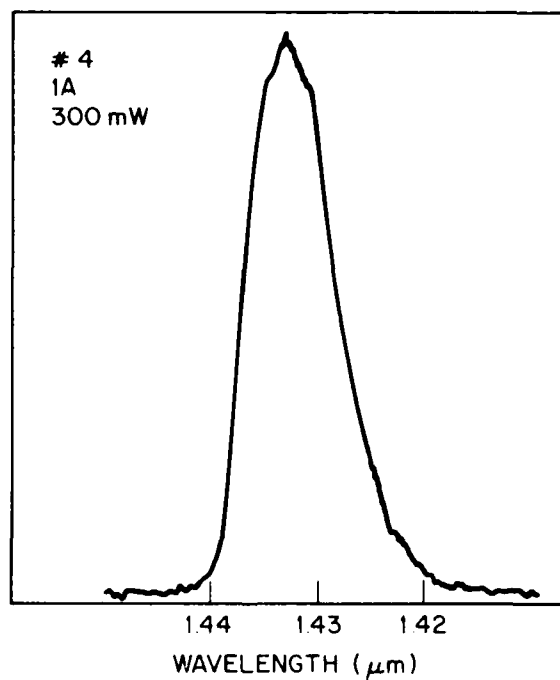


Figure 13. Emission spectrum of a typical 1.44-μm laser developed under contract.

square for InGaAsP. The others are the next lower square made by GaAs-InAs-InSb-GaSb, the next right square made by InAs-AlAs-AlSb-InSb, and the triangle region on the left of the bottom three square regions. The intercept points between these energy lines and substrate lines are marked 4, 5, and 6.

There are other regions of the same energies in the right side bottom corner, which are the triangle of AlSb-InSb-GaSb and the next lower square of GaSb-InSb-InP-GaP. In these two regions, the 0.64-eV lines intercept AlSb lines. Because of the difficulty in obtaining AlSb, no literature was found for such materials.

In the next left upper triangle of InAs-GaAs-AlAs, there are 0.64- and 0.496-eV regions. Although no substrate lines intercept with these energy lines, graded substrates can be useful, as described later. In this way, all the possible material combinations for longer wavelength regions were searched.

At the longer wavelengths, Auger recombination of the intervalence band absorption type often comes into discussion as the source of non-radiative recombination. The valence band separates into two levels due to spin orbit coupling. The top of the upper valence band has more holes when carriers are injected or the temperature is high. In this situation electrons can be excited from the lower valence band to the upper valence band. In long wavelength lasers, the regular bandgap value tends to be equal to the energy difference between the separated valence bands. In such a band configuration, radiation energy from the recombination of an electron-hole pair can be used for excitation of a carrier from the lower valence band to the upper valence band. Because of these nonradiative processes, a long wavelength laser often has a lower  $T_0$ , which means  $J_{th}$  is more influenced by temperature variations.

#### 4.3.1. AlGaAsSb/GaSb on GaSb Substrate

There are three triangles at the upper right side of the chart in Fig. 3. The square region below the central triangle of these three describes AlGaAsSb. The enlarged figure is shown in Fig. 14. The substrate line starts from the GaSb corner and has an energy range from 0.721 to 1.0 eV for the direct transition band. This corresponds to  $\lambda = 1.72$  to  $1.24 \mu\text{m}$  and does not cover the required wavelength. However, the published reports on this laser or detector structure [25,53-56] will help in actual growth processes for InGaAsSb/AlGaAsSb on GaSb, a useful structure described in the next section.

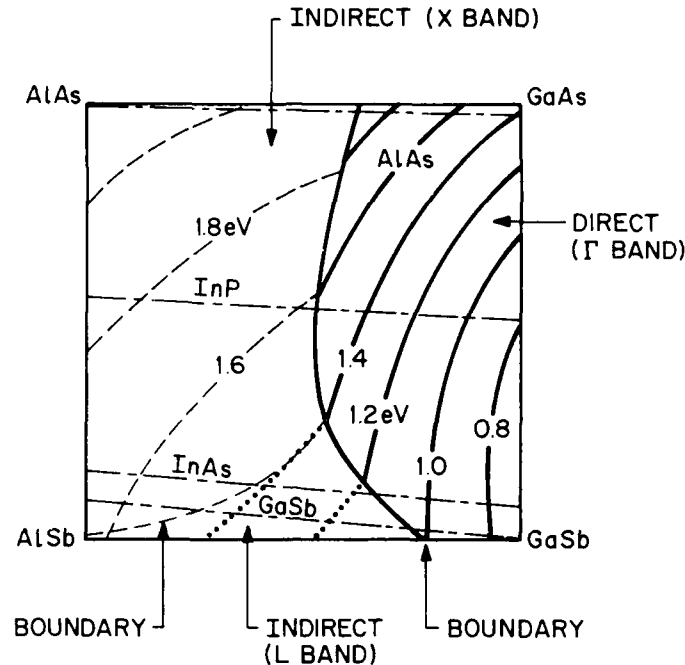


Figure 14. Energy bandgap diagram for AlGaAsSb.

#### 4.3.2. InGaAsSb/GaSb on GaSb Substrate

The square regions for InGaAsSb were extracted from Figs. 3 and 4 and enlarged as shown in Figs. 15(a) and (b). The two points are on the GaSb substrate line and the other two points are on the InAs substrate line. Each point corresponds to 1.93- or 2.5- $\mu\text{m}$  wavelength. When a point on these lines moves towards the GaSb region, the bandgap becomes larger, as seen in Fig. 15(a). However, the dielectric constant of the corresponding point also becomes larger, as seen in Fig. 15(b). This means the higher bandgap material has a higher refractive index, and suitable DH structures cannot be formed using InGaAsSb with different compositions.

Nevertheless, there are several reports that did not deal with the refractive index and presented a design for a DH structure [57-60]. DeWinter et al [58] describe an investigation on the miscibility gap in the  $\text{In}_x\text{Ga}_{1-x}\text{As}_y\text{Sb}_{1-y}$  growth solution. They point out that the miscibility gap region is for  $x > 0.22$ , and successful LPE growth on GaSb substrate was observed for the range of  $0 < x < 0.217$  where the corresponding photoluminescence covered the  $1.71 < \lambda < 2.3\text{-}\mu\text{m}$  range.



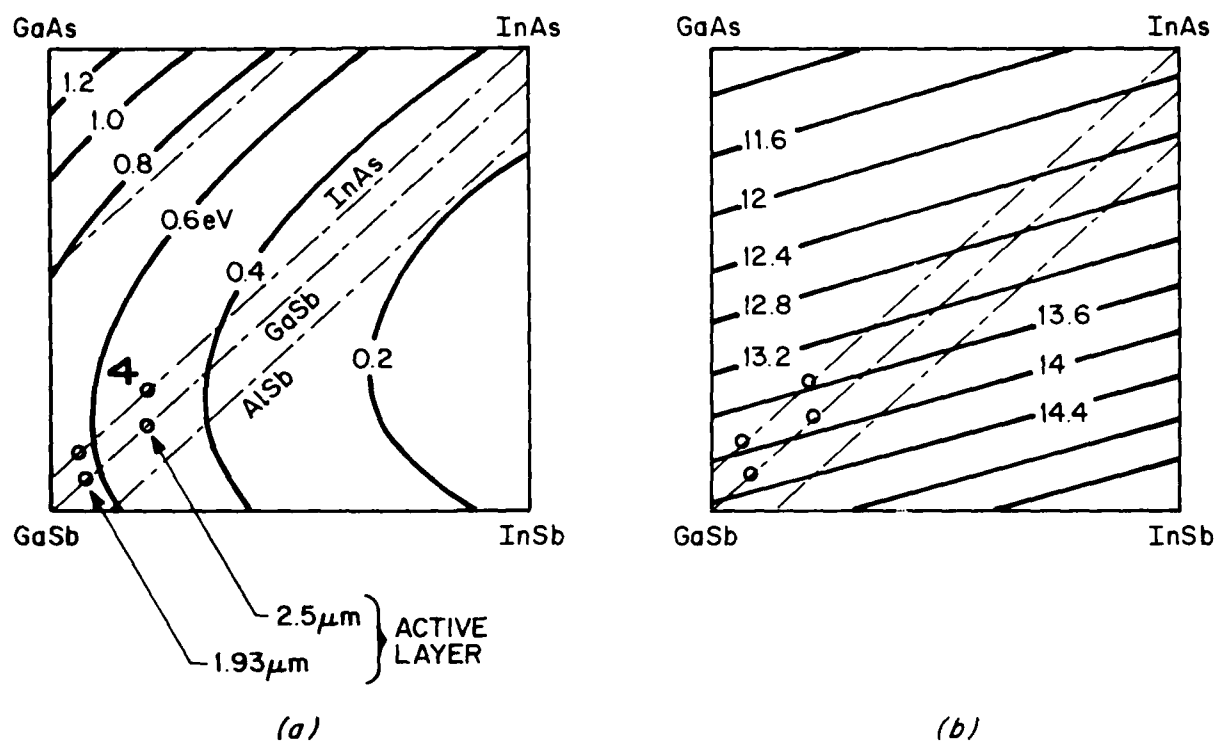


Figure 15. (a) Energy bandgap diagram for InGaAsSb and (b) Dielectric constant diagram for InGaAsSb.

An electron-beam-pumped laser using InGaAsSb grown on GaSb (no cladding) and InAs substrates showed a maximum wavelength of  $2.39 \mu\text{m}$  [61]. All the above InGaAsSb was grown by LPE and encountered the miscibility gap limitation. To reach the  $2.5\text{-}\mu\text{m}$  region, VPE or MOCVD may be used to exclude the miscibility gap problem.

#### 4.3.3. InGaAsSb/AlGaAsSb on GaSb

The material charts for InGaAsSb are shown in Fig. 15 and the chart for AlGaAsSb, in Fig. 14. The GaSb substrate line in the AlGaAsSb region covers 0.72- to 1.65-eV bandgap, which is larger than that of InGaAsSb, which covers 0.3 to 0.72 eV on the GaSb substrate line. Figure 15(b) illustrates that the dielectric constants of InGaAsSb in the 0.495- to 0.64-eV region on the GaSb substrate line are around 14, and it is possible to find a point with a smaller dielectric constant than 14 on the GaSb line in the AlGaAsSb square region. Therefore, DH structures can be designed.

N. Kobayashi et al [62, 63] reported InGaAsSb/AlGaAsSb on GaSb lasers with room-temperature pulse operation at a  $1.8\text{-}\mu\text{m}$  wavelength with  $J_{\text{th}} = 5 \text{ kA/cm}^2$ .

The threshold temperature characteristic was fairly good with  $T_0 = 112$  K, which is much larger than that of the InGaAsP 1.3- $\mu\text{m}$  laser, which is 53 to 57 K. They grew the laser by LPE. The range of wavelengths should cover 1.7 to 2.33  $\mu\text{m}$  (from photoluminescence [58]), while 2.39  $\mu\text{m}$  was observed by electron beam pumping [61]. If VPE or MOCVD is used, the miscibility gap problem will not appear and longer wavelength material can be grown.

C. Caneau et al [64] reported room temperature pulse operation of InGaAsSb/AlGaAsSb on a GaSb laser with  $J_{th} = 6.9 \text{ kA/cm}^2$  and  $T_0 = 85$  K, at  $\lambda = 2.2 \mu\text{m}$ , which is the longest wavelength reported in injection lasers using this material. The active layer thickness was not optimized at that time. After optimization, they expect room-temperature cw operation.

B. V. Dutt et al [65] reported a method to avoid difficulties in uniform growth of AlGaAsSb on GaSb and investigated a photon-pumped InGaAsSb/AlGaAsSb laser at 2.02~2.07  $\mu\text{m}$ . They investigated the temperature dependence in the 10- to 50°C range and obtained  $T_0 = 65$  K. Another report [66] describes only LPE growth condition for the InGaAsSb/AlGaAsSb on GaSb substrate.

#### 4.3.4. InAsSbP/InAsSbP on InAs

The material chart for InAsSbP is given by the lowest of the three triangles in the left side of Fig. 3. The enlarged chart is shown in Fig. 16. Two points are seen on the InAs substrate line where the energies are at 0.64 and 0.496 eV, which express material composition for 1.93- and 2.5- $\mu\text{m}$  lasers. The cladding materials should be on a point on the same line, but on a higher energy side. When a point for the cladding material falls on the corresponding point in the dielectric constant chart, the dielectric constant is lower for the higher energy side. Therefore, an appropriate DH structure can be designed. Although GaSb can provide a lattice matched substrate, meltback of substrate in the LPE process will probably occur because of differences in the melt solvent. Therefore, InAs should be used for the substrate.

All the published works on this material describe 3- to 4- $\mu\text{m}$  lasers (0.3- to 0.4-eV bandgap). But it is possible to modify the system for 1.93 to 2.5  $\mu\text{m}$ . The observed high threshold current and strong temperature dependence in the 3- to 4- $\mu\text{m}$  lasers were attributed to Auger recombination. If the bandgap is increased to 0.5 to 0.64 eV, the bandgap value may be larger than the valence band splitting due to spin orbit coupling, and nonradiative recombination may be reduced.

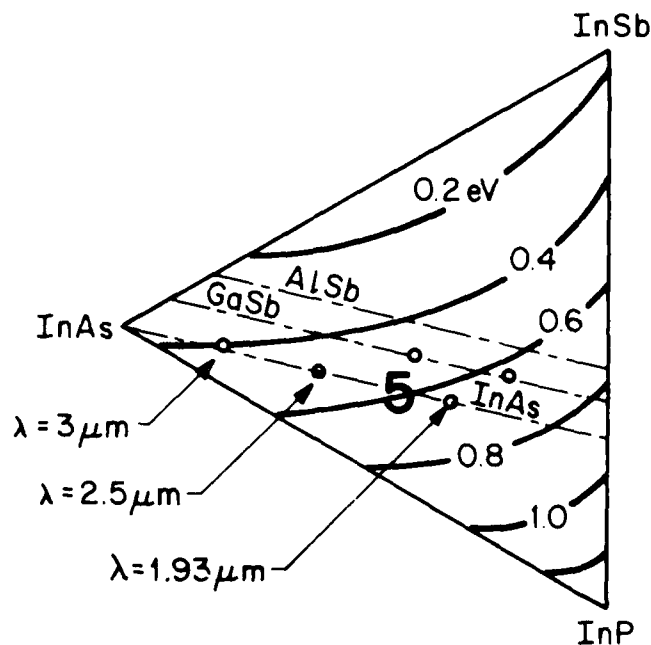


Figure 16. Energy bandgap diagram for InAsSbP.

N. Kobayashi et al [67] reported a 3- $\mu\text{m}$  laser operated at 77 K with  $J_{\text{th}} = 3 \text{ kA/cm}$ . The threshold current was very sensitive to temperature, with  $T_0 = 23 \text{ K}$ . The measurement was done up to 145 K. N. P. Esina et al [68] observed lasing action at 300 K. They compared the output power for different devices ranging from  $\lambda = 3.5$  to  $4.6 \mu\text{m}$ , and they observed that the output power dramatically increases with increasing bandgap in the 0.272- to 0.305-eV range as seen in Fig. 17, suggesting the reduction of nonradiative recombination. Therefore, there is a possibility that fairly good lasers may be realized in the 1.93- to 2.5- $\mu\text{m}$  range.

There are two papers on LPE growth condition [63,69].

#### 4.3.5. Various Ternary Materials on Graded Lattice Constant Substrate

In Fig. 3, ternary materials are expressed by straight lines between two adjacent binaries, or sides of triangles or squares. If a composition of a ternary is specified to produce a certain lasing wavelength, the lattice constant is automatically determined, so that it is impossible to control bandgap and lattice constant independently. Therefore, a mismatched substrate is generally used whose lattice constant is close to that of the laser materials,

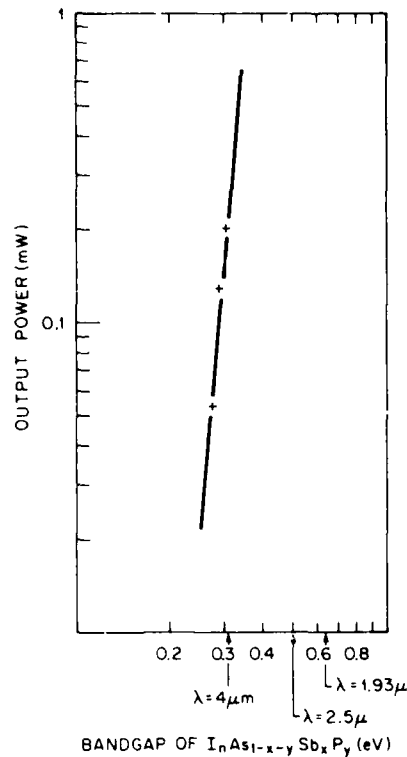


Figure 17. Output power vs bandgap of InAsSbP on InAs.

and intermediate layers are inserted whose lattice constant gradually varies from the substrate lattice constant to that of the laser material.

Generally, a graded substrate has some internal mechanical strain and misfit dislocations. This leads to relatively short life and less reliability compared to a lattice-matched substrate device. However, the present requirement is for high-power pulse operation, and long-life stability is not required. Furthermore, control of the growth process of ternaries is easier than that of the quaternaries because of fewer components. Also, the quality of the grown layer is sometimes superior to that of quaternaries. Therefore, a ternary DH structure using a graded substrate must also be considered. Possible ternaries for 1.93- and 2.5- $\mu\text{m}$  active layers are InGaAs, InGaSb, InAlAs, InAlSb, InAsP, and InSbP, and there are no other possibilities.

There are several reports on ternary lasers. C. J. Nuese et al at RCA [70,71] reported cw room-temperature InGaAs/InGaP lasers, and R. E. Nahory [72,73] reported GaAsSb/AlGaAsSb. Both have  $\sim 1\text{-}\mu\text{m}$  wavelength, and the structure cannot be modified to 1.93 or 2.5  $\mu\text{m}$  just by changing the component ratio.

H. Tamkin et al [74] and A. F. S. Penna [75] reported  $\text{In}_{0.53}\text{Ga}_{0.47}\text{As}/\text{In}_{0.52}\text{Al}_{0.48}\text{As}$  lattice matched to InP, whose wavelength fortunately was very close to  $1.55\text{ }\mu\text{m}$ , which is necessary for fiber communication. This structure can be modified to  $1.93$  and  $2.5\text{ }\mu\text{m}$ . As seen in Fig. 18, which is the same as the central one of the three right upper triangles in Fig. 3, the necessary energy points of  $0.64$  and  $0.496\text{ eV}$  are found on the InGaAs ternary line (side of triangle).

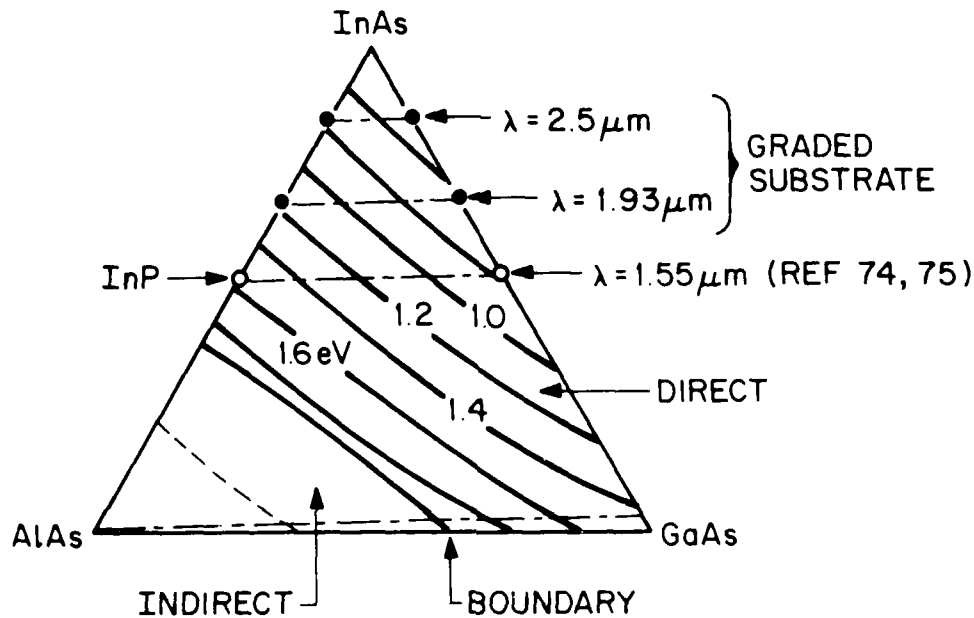


Figure 18. Energy bandgap diagram of InAlGaAs.

The constant lattice parameter line should be drawn from the  $0.64\text{-eV}$  point ( $1.93\text{-}\mu\text{m}$  active material) in parallel with the InP substrate line and the cladding material is found to be the  $1.17\text{-eV}$  point on the InAlAs ternary line. The graded intermediate layer has to be inserted between these laser materials and the substrate. The substrate material can be either InP or InAs. For a  $2.5\text{-}\mu\text{m}$  device, a point at  $0.496\text{ eV}$  on the InGaAs ternary line and another point at  $0.75\text{ eV}$  on InAlAs ternary line express active and cladding materials. In this case, the substrate should be InAs.

Among many possible ternaries, InGaAs/InAsP is a strong possibility. RCA, as well as other companies, has acquired a lot of experience with this material because of their interest in photodetectors using  $\text{In}_{0.57}\text{Ga}_{0.43}\text{As}$  designed for  $1.3$  to  $1.6\text{ }\mu\text{m}$ .

As seen in Fig. 19, InGaAs is expressed by the lower side line of the square region. There are two points, 0.64 and 0.495 eV, for active materials of 1.93 and 2.5  $\mu\text{m}$ . The points do not agree with the InP substrate line, which means both lattice constants do not match that of InP. The cladding materials should be determined from two intercept points between the vertical InAsP line and the lines extending from the two active material points in parallel with the InP substrate line. Examples of material parameters for the laser structures are shown in Table 3. One should note here that InAs may be used for the substrate for 2.5- $\mu\text{m}$  devices because the lattice constant is closer to that of the  $\text{In}_{0.82}\text{Ga}_{0.18}\text{As}$  active material than that of InP. However, InP can also be used.

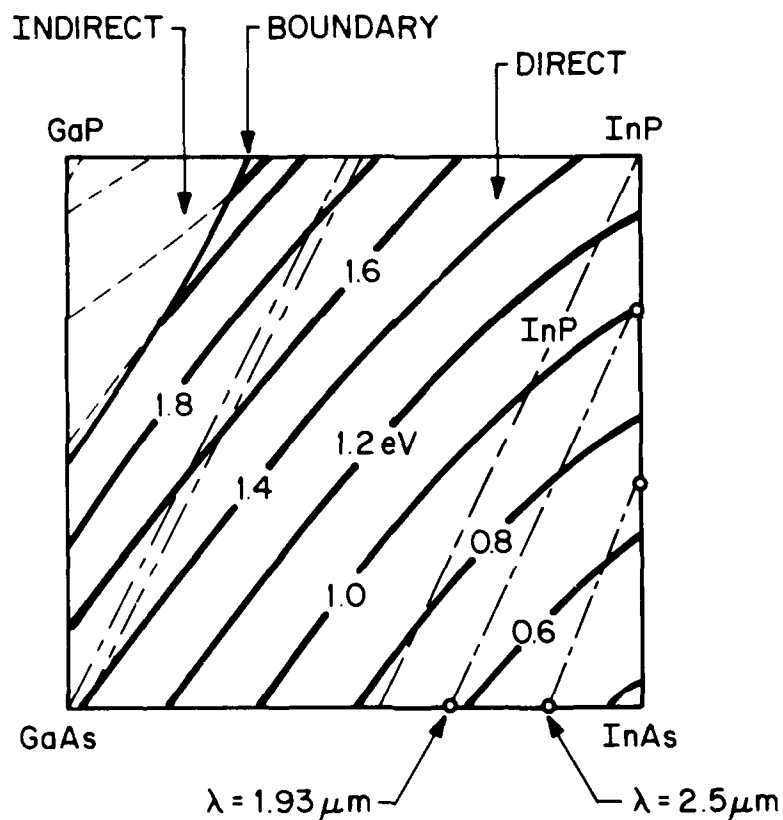


Figure 19. Energy bandgap diagram of InGaAsP.

TABLE 3. MATERIALS FOR LASERS

	Substrate	Graded Layer	Cladding	Active	Cladding
		In <sub>0.53</sub> Ga <sub>0.47</sub> As to			
Composition	InP	In <sub>0.62</sub> Ga <sub>0.38</sub> As	InAs <sub>0.18</sub> P <sub>0.82</sub>	In <sub>0.62</sub> Ga <sub>0.38</sub> As	InAs <sub>0.18</sub> P <sub>0.82</sub>
E <sub>g</sub> , eV	1.34		~1.1	0.642	~1.1
a <sub>0</sub> , Å	5.869	5.869-5.9	5.9	5.9	5.9
n	3.20		3.15	3.39	3.15
Doping, cm <sup>-3</sup>	2x10 <sup>18</sup> N	2x10 <sup>18</sup> N	1x10 <sup>18</sup> N	1x10 <sup>17</sup> N	2x10 <sup>18</sup> P
		InAs to			
Composition	InAs	In <sub>0.82</sub> Ga <sub>0.18</sub> As	InAs <sub>0.59</sub> P <sub>0.41</sub>	In <sub>0.82</sub> Ga <sub>0.18</sub> As	InAs <sub>0.59</sub> P <sub>0.41</sub>
E <sub>g</sub> , eV	0.359		0.7	0.495	0.7
a <sub>0</sub> , Å	6.058	6.058-5.99	5.99	5.99	5.99
n	3.44		3.3	3.41	3.3

## 5. DETECTORS

Properties required for photodetectors are:

- (1) high sensitivity at the wavelength of the light source,
- (2) wide frequency bandwidth,
- (3) low internal noise,
- (4) low dark current, and
- (5) high long-term operational reliability.

Devices with such properties are PIN photodiodes (PD) and avalanche photodiodes (APD).

The basic PIN photodiode structure is shown in Fig. 20. The  $p^+$  material has a wider bandgap so that the incident light passes through this window and surface recombination is suppressed. The PIN junction is reverse biased so that the photo-generated electrons in the I-layer are efficiently collected. The thickness of the I-layer is chosen so that the incident light is fully absorbed. For high-speed operation, the thickness of the I-layer may have to be made thinner to limit carrier transit-times with the depleted regions. The high field region quickly sweeps out the carriers.

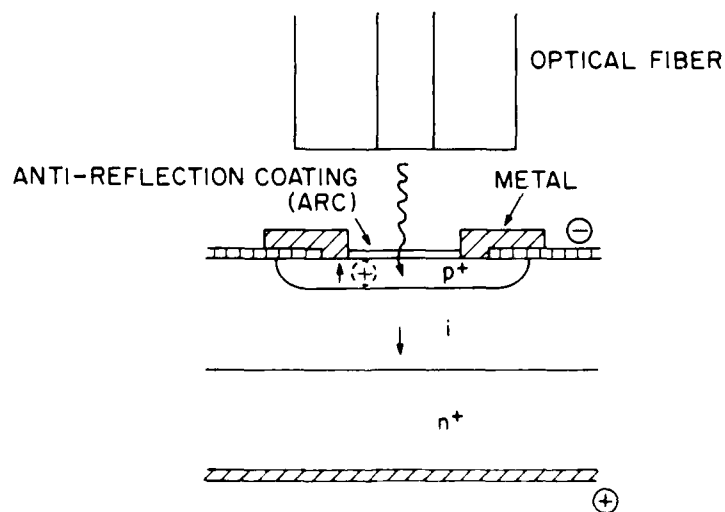


Figure 20. Structure of PIN photodetector.

The APD is also a reverse-biased, single-heterojunction device in which photogenerated carriers are avalanche multiplied in the pn junction region. Although the APD has more sensitivity than PIN-PD because of internal current



amplification, it generates more noise. The noise generation factor becomes maximum when  $\beta/\alpha = 1$ , and becomes lower when  $\beta/\alpha \gg 1$  or  $\beta/\alpha \ll 1$ , where  $\alpha$  is electron ionization rate and  $\beta$  is hole ionization rate.

The quantum efficiencies of various photodetectors [14] are shown in Fig. 21, and material parameters are shown in Table 4. The photosensitivities of all the materials have thresholds corresponding to the bandgap, as seen in Fig. 21. It is important to choose the optimum bandgap material not only for maximum sensitivity but also for minimum dark current. A laser material could work as a detector, but the bandgap must be somewhat less than that of the laser active layer. In addition, device performance has to be considered.

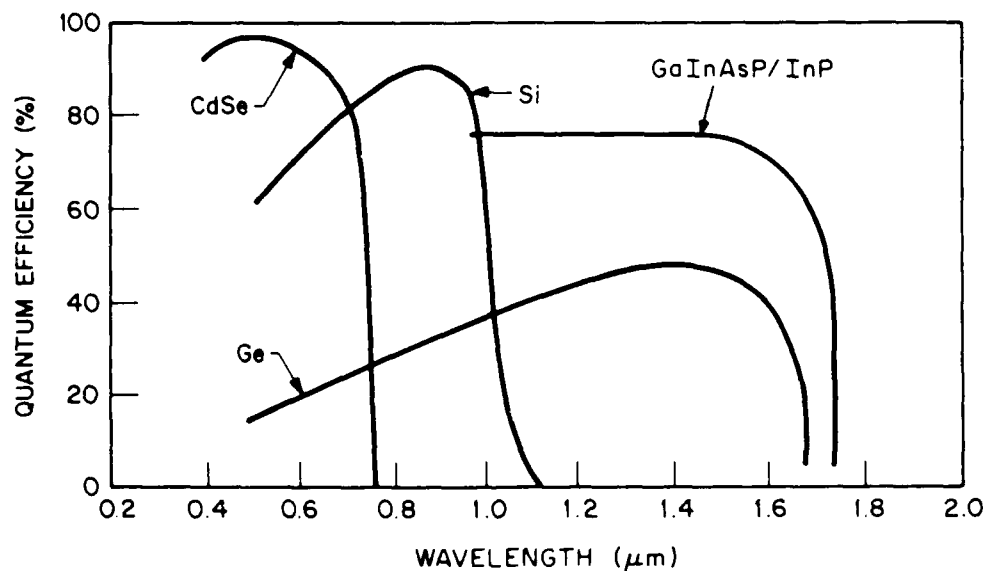


Figure 21. Quantum efficiency of various photodetectors using different materials.

### 5.1. 0.67-μm Devices

For the 0.67-μm range, Si PIN-PD or Si APD should work. The Si detector shows maximum quantum efficiency of 90% for PIN-PD and 50% for APD at  $\lambda = 0.9$  μm. The sensitivity at 0.67 μm decreases only by 15%. Since the Si detector is a homojunction device, the absorption coefficient becomes larger at 0.67 μm than at  $\lambda = 0.9$  μm. Therefore, it is desirable to design a thinner layer structure to improve the sensitivity at 0.67 μm. Si devices have the lowest dark current density, as seen in Table 4.

TABLE 4. MATERIALS FOR PHOTODETECTORS

Parameters	Material									
	$\text{Ga}_{1-x}\text{In}_x\text{As}_y\text{P}_{1-y}$ /InP	$\text{Ga}_{0.47}\text{In}_{0.53}\text{As}$ /InP	$\text{Ga}_{0.27}\text{In}_{0.73}\text{As}$ /InP	$\text{H}_{0.3}\text{Cd}_{0.7}\text{P}_{0.60}$	$\text{Al}_x\text{Ga}_{1-x}\text{As}_{1-y}\text{Sb}_y$ /GaSb	Ge	Si			
Bandgap (eV)	1.35 - 0.75	0.75	0.95	0.92	1.24 - 0.73	0.72	1.1			
Wavelength ( $\mu\text{m}$ )	0.92 - 1.67	1.67	1.30	1.35	1.0 - 1.7	1.72	1.1			
Mobility $\mu(\text{cm}^2/\text{Vsec})$	electron 3200 - 8500		5000			3900	1300			
	hole 70 - 180		80			1900	500			
Effective Mass $m_e/m_0$	$0.08 \sim 0.04$ ( $\lambda=0.92 \sim 1.67 \mu\text{m}$ )		$0.045 \sim 0.055$		$0.08$		$0.19$			
Dark Current [nA] [area: $4 \times 10^3 \mu\text{m}^2$ ]	$10^{-2} - 4 \times 10^{-1}$		$10^{-1}$	60	$10^2$	10	$10^{-4}$			
Ionization Rate	$\beta > \alpha$		$\beta > \alpha$	$\beta > \alpha$	$\beta > \alpha$	$\beta > \alpha$				
$(\beta/\alpha \text{ or } \alpha/\beta)$	$0.2 - 0.3$		0.25	0.03	$0.05 - 0.5$	0.5	0.2			
Sensitivity A/W	$0.6 - 0.8$		0.8	0.6	(0.6)	$0.85$				

### 5.2. 1.44- $\mu$ m Devices

For the 1.4- $\mu$ m range, materials with narrower bandgap than that of Si are necessary. Possible materials are Ge, InGaAsP, HgCdTe, AlGaAsSb (Table 3). For practical systems in the 1 to 1.7- $\mu$ m range, there are Ge APD [76] and  $\text{In}_{0.53}\text{Ga}_{0.47}\text{As}$  PIN-PD [77] or APD [78] and RCA  $\text{In}_{0.57}\text{Ga}_{0.43}\text{As}$  PIN-PDs. The Ge APD is a very useful device for optical communications, designed for the 1.3- and 1.55- $\mu$ m range. Its sensitivity and response speed are not inferior to those of Si APD, but the room temperature dark current density is  $10^5$  times larger than that of Si APD. Its excess noise factor is also larger because  $\alpha/\beta \approx 0.5$ . On the other hand,  $\text{In}_{0.53}\text{Ga}_{0.47}\text{As}/\text{InP}$  APD has a lower dark current density, and  $\beta/\alpha = 0.25$ . The PIN-PD is connected to a GaAs FET to obtain higher sensitivity [79] and is currently in use.

### 5.3. 1.93- and 2.5- $\mu$ m Devices

The detection of 1.93- or 2.5- $\mu$ m radiation is best achieved with compound InGaAs/InAsP photodiodes whose composition and, hence, bandgap, is optimized for maximal sensitivity. That is, the bandgap is made just large enough to absorb 1.93- $\mu$ m light efficiently. This strategy also minimizes the dark current in the device, since the dark current generally decreases with increasing bandgap in a high purity crystalline material. Thus, with maximal quantum efficiency and minimal dark current, the diode's sensitivity is optimal.

For example,  $\text{In}_{0.57}\text{Ga}_{0.43}\text{As}$  has a bandgap of 0.57 eV, which implies a detection threshold wavelength of 2.18  $\mu$ m. The absorption constant at 1.93  $\mu$ m is of the order of  $1 \mu\text{m}^{-1}$ , which means that 1.93- $\mu$ m radiation will be fully absorbed in the first few microns of the active layer. This implies a quantum efficiency of 60 to 80 percent, based on our experience with  $\text{In}_{0.57}\text{Ga}_{0.43}\text{As}$  1.3-1.6- $\mu$ m photodiodes.

Infrared detectors are available commercially, but they utilize binary III-V compounds such as InAs or InSb or ternary HgCdTe compounds. Their bandgaps are much smaller than 0.57 eV ( $E_g(\text{InAs}) = 0.36$  eV;  $E_g(\text{InSb}) = 0.17$  eV) and, hence, they have high dark currents. Some require cooling. Because our ternary III-V compound photodiodes have the largest possible bandgap, they will have lower dark currents, and therefore, better sensitivity than the commercial units at any temperature.

For 1.3- and 1.5- $\mu\text{m}$  light, a PIN photodetector having the structure shown in Fig. 22 is used. These diodes are presently a commercial product from the RCA New Products Division. Typically, they have quantum efficiencies of 75% at 1.3  $\mu\text{m}$  and 80% at 1.55  $\mu\text{m}$ , with dark leakage currents of less than 10 nA for a 100  $\mu\text{m}$  diameter mesa diode.

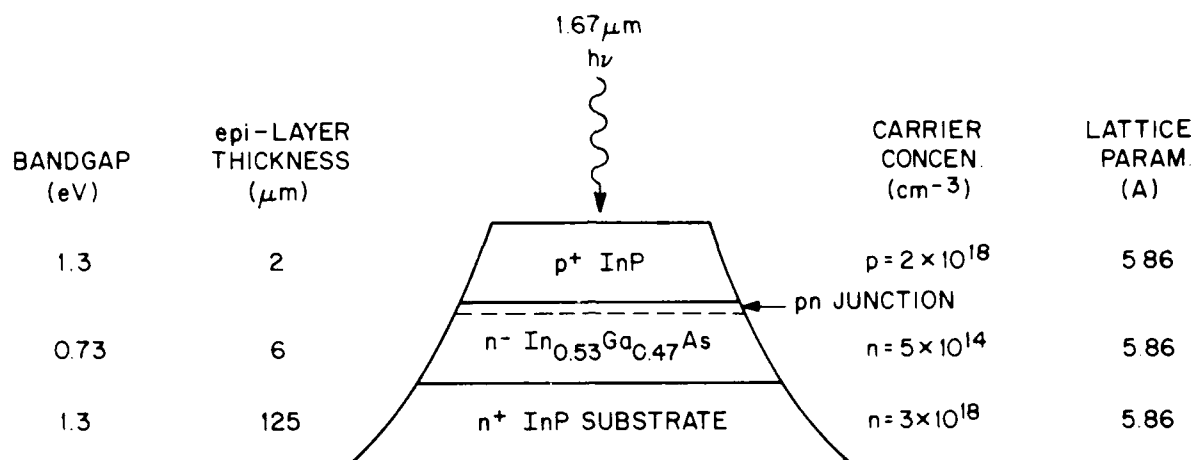


Figure 22. Structure of PIN photodetector using InGaAs heterojunction of RCA product

As discussed above, the bandgap of the InGaAs alloy must be optimized for 1.93- and 2.5- $\mu\text{m}$  detectors. However, for these wavelengths, this alloy cannot be lattice matched as a heterojunction to an InP or an InAs substrate. Rather, the alloy must be graded in composition from either InP ( $a = 5.87 \text{ \AA}$ ) or InAs ( $a = 6.05 \text{ \AA}$ ). An example of a proposed 1.93- $\mu\text{m}$  detector is shown in Fig. 23. The grading procedure has been used in other optoelectronic devices at RCA and is a well-proven technology. The composition can be either continuously or step graded from the substrate to the  $\text{In}_{0.70}\text{Ga}_{0.30}\text{As}$  constant composition l-layer. This alloy has a lattice parameter of 5.936  $\text{\AA}$  and a bandgap of 0.57 eV, which corresponds to a wavelength of 2.17  $\mu\text{m}$  (the bandgap must be about 0.070 eV less than the laser emission for efficient absorption and detection). The carrier concentration should be as low as possible to achieve low capacitance devices, necessary for sensitive, high-speed detector systems.

The  $p^+$  layer forms part of the p-n junction for the collection of the photo-generated carriers. For present RCA photodetectors, zinc from the zinc-doped InP cap layer diffuses during vapor growth about 0.5  $\mu\text{m}$  into the InGaAs l-layer. The InP cap is a high bandgap layer that acts as a window to pass the 1.55- $\mu\text{m}$

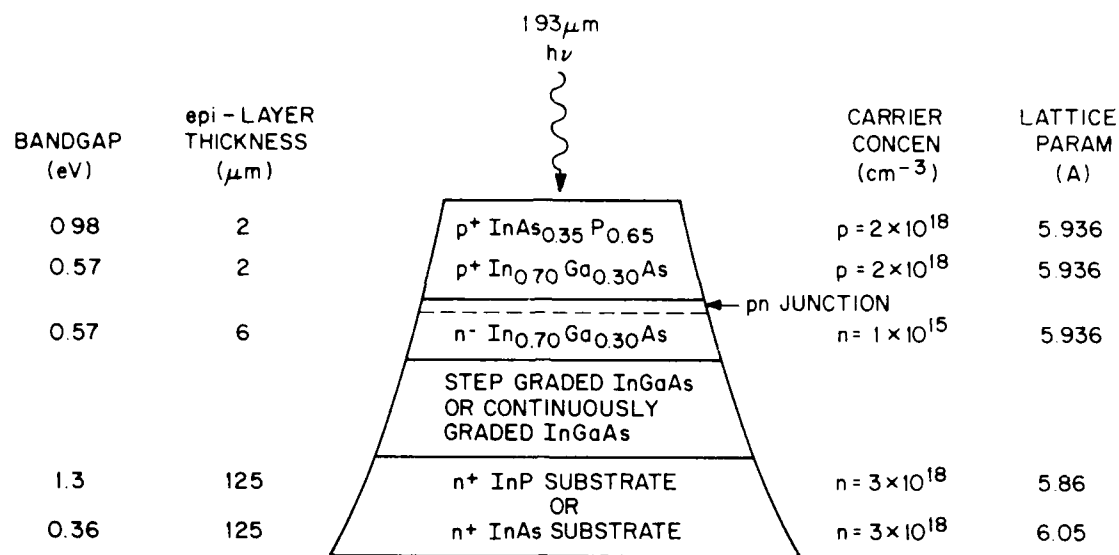


Figure 23. Proposed structure of PIN photodetector using InGaAs on graded substrate.

light and also reduces surface recombination of photogenerated carriers to increase the detection efficiency. For the proposed  $\text{In}_{0.70}\text{Ga}_{0.30}\text{As}$  I-layer, the capping  $p^+$ -layer can be an  $\text{InAs}_{0.35}\text{P}_{0.65}$  alloy, which has the same lattice parameter as the  $\text{In}_{0.70}\text{Ga}_{0.30}\text{As}$  I-layer and has a larger bandgap, 0.98 eV.

The proposed structure of 2.5-μm detectors is almost the same as that for 1.93-μm devices except for the material compositions, which are  $\text{In}_{0.89}\text{Ga}_{0.11}\text{As}$  for the I-layer and  $\text{InAs}_{0.78}\text{P}_{0.22}$  for the cap layer.

## 6. CONCLUSIONS

Appropriate high-power pulse laser structures at 0.67-, 1.44-, 1.93-, and 2.5- $\mu\text{m}$  wavelengths were investigated mainly from the materials combination point of view through discussions, from published reports, and by new analyses.

For  $\sim 0.67\text{-}\mu\text{m}$  devices, the technology is rapidly growing and various encouraging results have been reported recently.

The best result is cw room temperature operation with very low threshold current of  $4.1\text{ kA/cm}^2$  using  $\text{In}_{0.5}\text{Ga}_{0.5}\text{P}/(\text{Al}_{0.4}\text{Ga}_{0.6})_{0.5}\text{In}_{0.5}\text{P}$  at  $\lambda = 0.69\text{ }\mu\text{m}$ .

Also, 30-mW power output at room-temperature pulse operation was reported using  $\text{In}_{0.47}\text{Ga}_{0.53}\text{As}_{0.05}\text{P}_{0.95}/\text{Al}_{0.6}\text{Ga}_{0.4}\text{As}$  at  $\lambda = 0.67\text{ }\mu\text{m}$ .

Another possibility is an  $\text{Al}_{0.35}\text{Ga}_{0.65}\text{As}/\text{Al}_{0.5}\text{Ga}_{0.5}\text{As}$  multiple quantum well laser in which the threshold current was as low as that of the 0.73- $\mu\text{m}$  AlGaAs laser.

For 1.44- $\mu\text{m}$  lasers, the technologies of 1.3- and 1.55- $\mu\text{m}$  devices are well established and were modified for the composition. Real devices that produced 700-mW output power for 1.7 A, 400-ns pulse operation at room temperature were successfully fabricated.

For the longer wavelengths of 1.93 and 2.5  $\mu\text{m}$ , a new graded-substrate scheme was proposed, in which InGaAs/InAsP is grown on InGaAs graded layer on InP or InAs substrate. InGaAsSb/AlGaAsSb on GaSb was reported to lase at 1.8  $\mu\text{m}$  with  $J_{\text{th}} = 5\text{ kA/cm}^2$  and  $T_0 = 112\text{ K}$ . The same active material showed a maximum wavelength at 2.39  $\mu\text{m}$ . This is on the boundary of the miscibility gap for LPE growth, and the temperature rise might increase the wavelength up to 2.5  $\mu\text{m}$ . Another possibility is to use vapor phase growth, in which the miscibility gap does not limit the growth.

## REFERENCES

1. M. I. Nathan, W. P. Dumke, G. Burn, F. H. Dills, Jr. and Laher, "Stimulated Emission of Radiation from GaAs p-n Junctions," Appl. Phys. Lett., 1, 3, p. 62 (1962).
2. M. Quist, R. H. Rediker, R. J. Keyes, W. E. Krag, B. Lax, A. L. McWhorter and H. J. Zeiger, "Semiconductor Maser of GaAs," Appl. Phys. Lett., 1, 4, p. 91 (1962).
3. R. N. Hall, G. H. Fenner, J. D. Kingsley, T. J. Soltys and R. D. Carlson, "Coherent Light Emission from GaAs Junctions," Phys. Rev. Lett., 9, 366 (1962).
4. H. Kressel and H. Nelson, "Closed-Confinement Gallium Arsenide PN Junction Lasers with Reduced Optical Loss at Room Temperature," RCA Review, 30, p. 106 (1969).
5. I. Hayashi, M. B. Panish, P. W. Foy and A. Sumski, "Junction Lasers which Operate Continuously at Room Temperature," Appl. Phys. Lett., 17, 3, p. 109 (1970).
6. H. Yonezu, I. Sakuma, T. Kamejima, M. Heno, K. Nishida, Y. Nannichi and I. Hayashi: Degradation Mechanism of (AlGa)As Double Heterostructure Laser Diodes," Appl. Phys. Lett., 24, 1, p. 18 (1974).
7. B. C. Deloach, Jr., B. W. Hakki, R. I. Hartman and I. A. D'Asaro: Degradation of CW GaAs Double Heterojunction Lasers at 300 K," Proc. IEEE (Lett.), 61, p. 1042 (1973).
8. D. Petrott and R. I. Hartman: Rapid Degradation Phenomenon in Heterojunction GaAlAs-GaAs Lasers," J. Appl. Phys., 45, 9, p. 3899 (1974).
9. T. Kobayashi, T. Kawakami and Y. Furukawa: Thermal Diagnosis of Dark Lines in Graded GaAs/GaAlAs Double Heterostructure Lasers," Japan J. Appl. Phys., 14, 4, p. 508 (1975).
10. H. Kan, H. Namizaki, M. Ishii and A. Ito: Continuous Operation over 10000h of GaAs/GaAlAs Double-Heterostructure Laser without Lattice Mismatch Compensation, Appl. Phys. Lett., 27, 4, p. 138 (1975).
11. Y. Nannichi, J. Matsui and K. Ishida: Rapid Degradation in Double Heterostructure Lasers, II," Japan J. Appl. Phys., 14, 10, p. 1561 (1975).
12. S. Kishino, H. Nakashima, N. Chinone and R. Ito, "X-ray Topographic Observation of Dark-Line Defects in GaAlAs Double-Heterostructure Wafers," Appl. Phys. Lett., 28, 2, p. 98 (1976).

13. W. B. Joyce, R. W. Dixon and R. L. Hartman, "Statistical Characterization of the Lifetimes of Continuously Operated (Al,Ga)As Double-Heterostructure Lasers," Appl. Phys. Lett., 28, 11, p. 684 (1976).
14. Y. Suematsu, Semiconductor Lasers and Integrated Optics, Ohm Publishing Co., Tokyo, 1984 (Japanese).
15. T. Okoshi, Optical Fibers, Academic Press, New York (1982).
16. K. Noda, "Optical Fiber Transmission," Institute of Electronics and Communication Engineer of Japan (1984).
17. H. Kressel and J. K. Butler, Semiconductor Lasers and Heterojunction LEDs, Academic Press (1977).
18. H. C. Casey, Jr., "Room Temperature Threshold-Current Dependence of GaAs-Al<sub>x</sub>Ga<sub>1-x</sub>As Double-Heterostructure Lasers on x and Active Layer Thickness," J. Appl. Phys., 49, 3684 (1978).
19. N. Kamata, T. Kamiya and H. Yanai, "Direct Observation of Carrier Leakage Through Hetero-Barriers In a Highly Excited AlGaAs DH LED," Int. Symp. Gallium Arsenide and Related Compounds, 1981 Japan Inst. Phys. Conf., 63, 497 (1982).
20. S. Yamakoshi, T. Sanada, O. Wada, I. Umebu and T. Sakurai, "Effect of Carrier Leakage on InGaAsP/InP Double Heterostructure Light Emitters," Int. Symp. Gallium Arsenide and Related Compounds, 1981 Japan Inst. Phys. Conf. Ser. 63, 485 (1982).
21. J. Shah, R. F. Leheny, R. E. Nahory and H. Temkin, "Hot-Carrier Effect in 1.3  $\mu$  In<sub>1-x</sub>Ga<sub>x</sub>As<sub>y</sub>P<sub>1-y</sub> Light Emitting Diodes," Appl. Phys. Lett., 39, 618 (1981).
22. A. R. Adams, M. Asada and Y. Suematsu, "Dependence of the Efficiency and Threshold Current of In<sub>1-x</sub>Ga<sub>x</sub>As<sub>x</sub>P<sub>1-x</sub> Lasers Related to Intervalence Band Absorption," Japan J. Appl. Phys., 19, L621 (1980).
23. H. Kan, H. Namisaki, M. Ishii and A. Ito, "Continuous Operation over 1000 h of GaAs-AlGaAs Double-Heterostructure Laser Without Lattice Mismatch Compensation," Appl. Phys. Lett., 27, 138 (1975).
24. H. Yonezu, M. Ueno, T. Kamejima and H. Hayashi, "An AlGaAs Window Structure Laser," IEEE J. Quantum Electron, QE-15, 775 (1979).
25. A. Sasaki, M. Nishiuma, Y. Takeda, "Energy Band Structure and Lattice Constant Chart of III-V Mixed Semiconductors and AlGaAs/AlGaAsSb Semiconductor Lasers on GaSb Substrates," Japanese J. Appl. Phys., 19, 1695 (1980).



26. J. Pankove, *Optical Process in Semiconductors*, Dovers, New York, (1971), p. 89.
27. T. S. Moss, *Optical Properties of Semiconductors*, Butterworth (1950), p. 48.
28. I. Hino, A. Gomyo, K. Kobayashi, T. Suzuki, K. Nishida, "Room Temperature Pulsed Operation of AlGaInP/GaInP/AlGaInP Double Heterostructure Visible Laser Diodes Grown by Metalorganic Chemical Vapor Deposition," *Appl. Phys. Lett.*, **43**, 987 (1983).
29. H. Asahi, Y. Kawamura, H. Nagai, "Molecular Beam Epitaxial Growth of InGaAlP Visible Laser Diode Operating at 0.66-0.68  $\mu\text{m}$  at Room Temperature," *J. Appl. Phys.*, **54**, 6958 (1983).
30. K. Kobayashi, I. Hino, T. Suzuki, "626.2-nm Pulsed Operation (300 K) of an AlGaInP Double Heterostructure Laser Grown by Metalorganic Chemical Deposition," *Appl. Phys. Lett.*, **46**, 7 (1985).
31. K. Kobayashi, S. Kawata, A. Gomyo, I. Hino, T. Suzuki, "Room-Temperature CW Operation of AlGaInP Double-Heterostructure Visible Lasers," *Electronic Letts.*, **21**, 931 (1985).
32. T. Suzuki, I. Hino, A. Gomyo and K. Nishida, "MOCVD-Grown  $\text{Al}_{0.5}\text{In}_{0.5}\text{P}$ - $\text{Ga}_{0.5}\text{In}_{0.5}\text{P}$  Double Heterostructure Lasers Optically Pumped at 90°K," *Japan J. Appl. Phys.*, **21**, L731 (1982).
33. I. Hino, K. Kobayashi and T. Suzuki, "High Aluminum Composition AlGaInP Grown by Metalorganic Chemical Vapor Deposition - Impurity Doping and 590 nm (Orange) Electroluminescence," *Japan J. Appl. Phys.*, **23**, L746 (1984).
34. J. A. Van Vechten, "Quantum Dielectric Theory of Electronegativity in Covalent Systems Electronic Dielectric Constant," *Phys. Rev.*, **182** 891 (1969).
35. K. Kishino, Y. Kozumi, A. Yokochi, S. Kinoshita and T. Tako, "0.67  $\mu\text{m}$  Room Temperature Operation of GaInAsP/AlGaAs Lasers on GaAs Prepared by LPE," *Japan J. Appl. Phys.*, **23**, L740 (1984).
36. K. Kishino, Y. Kaneko and A. Harada, "CW operation of 0.67  $\mu\text{m}$  GaInAsP/AlGaAs Laser at 208 K Grown on GaAs Substrates by LPE," *Japan J. Appl. Phys.*, **24**, L358 (1984).
37. K. Oe, S. Ando and H. Asai, "Liquid Phase Epitaxial Growth of GaInP/AlGaAs Double Heterostructures for Visible Lasers," *J. Cryst. Growth*, **64**, 309 (1984).

38. S. Mukai, H. Yajima, J. Shimada, "Fabrication and Visible-Light-Emission Characteristics of Room-Temperature-Operated InGaPAs DH Diode Lasers Grown on GaAs Substrate," Japanese J. Appl. Phys., 20, L729 (1981).
39. H. Kressel, C. J. Nuese and G. H. Olsen, "Red-Emitting Ga(AsP)/(InGa)P Heterojunction Lasers," J. Appl. Phys., 49, 3140 (1978).
40. A. Usui, T. Matsumoto, M. Inai, I. Mito, K. Kobayashi, H. Watanabe, "Low Threshold Current Operation of Vapour-Grown 650 nm-Band InGaAsP/InGaP DH Lasers," Elec. Lett., 21, 54 (1985).
41. M. Shimura, A. Fujimoto, H. Yasuda, S. Yamashita, "LPE Growth and Pulsed Room Temperature Laser Operation of  $\text{In}_{1-x}\text{Ga}_x\text{As}_z\text{P}_{1-z}$  on  $(100)\text{GaAs}_{1-y}\text{P}_y$  ( $y \approx 0.39$ )," Japanese J. Appl. Phys., 21, L338 (1982).
42. S. W. Kirchoefer, E. A. Rezek, B. A. Vojak, N. Holonyak, JR., D. Finn, D. L. Keune and J. A. Rossi "Continuous Room Temperature photopumped Laser Operation of Visible - Spectrum LPE  $\text{In}_{1-x}\text{Ga}_x\text{P}_{1-z}\text{As}_z$  ( $\lambda \sim 6700\text{\AA}$ )." IEEE J. Quantum Elec. QE-17 161 (1981).
43. S. Yamamoto, H. Hayashi, T. Hayakawa, N. Miyauchi, S. Yano and T. Hijikata, "680 nm CW Operation at Room Temperature by AlGaAs Double Heterojunction Lasers," IEEE J. Quantum Elec., QE-19, 1009 (1983).
44. T. Kajimura, T. Kuroda, S. Yamashita, N. Nakamura and J. Umeda, "Transverse-Mode Stabilized  $\text{Ga}_{1-x}\text{Al}_x\text{As}$  Visible Diode Lasers," Appl. Opt., 18, 1812 (1979).
45. I. Ladany and H. Kressel, "Visible CW (AlGa)As Heterojunction Laser Diodes," IEEE Int. Electron Device Mtg. Tech. Digest, p. 129, Washington, DC (1976).
46. W. T. Tsang, "Infrared-Visible ( $0.89\text{-}0.72\text{ }\mu\text{m}$ )  $\text{Al}_x\text{Ga}_{1-x}\text{As}/\text{Al}_y\text{Ga}_{1-y}\text{As}$  Double Heterostructure Lasers Grown by Molecular Beam Epitaxy," J. Appl. Phys., 51, 917 (1980).
47. T. Saku, H. Iwamura, Y. Hirayama, Y. Suzuki and H. Okamoto, "Room Temperature Operation of 650 nm AlGaAs Multi-Quantum-Well Laser Diode Grown by Molecular Beam Epitaxy," Japanese J. Appl. Phys., 24, L73 (1985).
48. N. Holonyak, Jr., R. M. Kolbas, R. D. Dupuis and P. D. Dapkus, "Quantum-Well Heterostructure Lasers," IEEE J. Quantum Elec., QE-16, 170 (1980).
49. R. D. Burnham, W. Streifer, T. L. Paoli and N. Holonyak, Jr., "Growth and Characterization of AlGaAs/GaAs Quantum Well Lasers," J. Crystal Growth, 68, 370 (1984).

50. R. D. Dupuis, P. D. Dapkus, N. Holonyak, Jr. and R. M. Kolbas, "Continuous Room Temperature Multiple-Quantum-Well  $\text{Al}_{1-x}\text{Ga}_x\text{As-GaAs}$  Injection Lasers Grown by Metalorganic Chemical Vapor Deposition," *Appl. Phys. Lett.*, **35**, 487 (1979).
51. D. R. Scifres, R. D. Burnham, C. Lindstrom, W. Streifer and T. L. Paoli, "Phase-Locked (GaAl)As Laser Emitting 1.5 W cw per Mirror," *Appl. Phys. Letts.*, **42**, 645 (1983).
52. D. R. Scifres, C. Lindström, R. D. Burnham, W. Streifer and T. L. Paoli, "Phase-Locked (GaAl)As Laser Diode Emitting 2.6 W cw from a Single Mirror," *Electron. Lett.*, **19**, 169 (1983).
53. W. T. Tsang, N. A. Olsson, "Preparation of 1.78  $\mu\text{m}$  Wavelength  $\text{Al}_{0.2}\text{Ga}_{0.8}\text{Sb/GaSb}$  Double Heterostructure Lasers by Molecular Beam Epitaxy," *Appl. Phys. Lett.*, **43**, 8 (1983).
54. L. M. Dloginov, A. E. Drakin, L. V. Druzhinina, P. G. Eliseev, M. G. Milvidsky, V. A. Skripkin and B. N. Sverdlov, "Low Threshold Heterojunction AlGaAsSb/GaSb Lasers in the Wavelength Range of 1.5-1.8  $\mu\text{m}$ ," *IEEE Quantum Electron.*, **QE-17**, 593 (1981).
55. H. D. Law, R. Chin, K. Nakano and R. A. Milano, "The GaAlAsSb Quaternary and GaAlSb Ternary Alloy and Their Application to Infrared Detectors," *IEEE J. Quantum Electron.*, **QE-17**, 275 (1981).
56. R. Chin, H. D. Law and K. Nakano, "GaAlAsSb/GaSb Avalanche Photodetectors," *SPIE Vol. 272, High Speed Photodetectors*, 11 (1981).
57. L. M. Dolginov, L. V. Druzhinina, P. G. Eliseev, I. V. Kryukova, V. I. Leskovich, M. G. Milvidskii, B. V. Sverdlov, E. G. Shevchenko, "Multicomponent Solid Solution Semiconductor Lasers," *IEEE J. Quantum Elect.*, **QE-13**, 609 (1977).
58. J. C. DeWinter, M. A. Pollak, A. K. Srivastava, J. L. Zyskind, "Liquid Phase Epitaxial  $\text{Ga}_{1-x}\text{In}_x\text{As}_{1-y}\text{Sb}_y$  Lattice Matched to (100) GaSb over the 1.71 to 2.33  $\mu\text{m}$  Wavelength Range," *Electron. Material Conf. Digest, Colorado Session: Vapour Phase Epitaxy*, June 20, 1985, p. 95.
59. L. M. Dolginov, L. V. Druzhinina, P. G. Eliseev, A. N. Lapshin, M. G. Milvidskii and B. N. Sverdlov, "Injection Heterolaser Based on InGaAsSb Four-Component Solid Solution," *Sov. J. Quantum Electron.*, **8(3)**, 416 (1978).
60. H. Kano and K. Sugiyama, "2.0 mW CW Operation of GaInAsSb/GaSb DH Lasers at 80 K," *Elect. Letts.*, **16**, 146 (1980).

61. L. M. Dolginov, L. V. Druzhinina, I. V. Kryukova, A. N. Lapshin, V. I. Leskovich, E. V. Matveenko and M. G. Milvidskii, "Efficient Room-Temperature Stimulated Emission from a  $\text{Ga}_x\text{In}_{1-x}\text{As}_y\text{Sb}_{1-y}$  Semiconductor Laser in the Spectral Range 1.8-2.4  $\mu$ ," Sov. J. Quantum Electron., 8(1), 66 (1978).
62. N. Kobayashi, Y. Horikoshi and C. Uemura, "Room Temperature Operation of the InGaAsSb/AlGaAsSb DH Laser at 1.8  $\mu$ m Wavelength," Japanese J. Appl. Phys., 19, L30 (1980).
63. N. Kobayashi, Y. Horikoshi and C. Uemura, "Semiconductor Materials for 2-4  $\mu$ m Region Optical Sources and Room Temperature Operation of InGaAsSb/AlGaAsSb DH Lasers," Proc. 4th Int. Conf. Ternary and Multinary Compounds, Tokyo, 1980, Japanese J. Appl. Phys., 19, 333 (1980).
64. C. Caneau, A. K. Srivastava, A. G. Dentai, J. L. Zyskind, M. A. Pollack, "Room Temperature GaInAsSb/AlGaAsSb DH Injection Lasers at 2.2  $\mu$ m," Electron. Letts., 21, 815 (1985).
65. B. V. Dutt, H. Temkin, E. D. Kolb, W. A. Sunder, "Room Temperature Operation of Optically Pumped InGaAsSb/AlGaAsSb Double-Heterostructure Lasers at  $\approx 2$   $\mu$ m," Appl. Phys. Lett., 47, 111 (1985).
66. N. Kobayashi, Y. Horikoshi and C. Uemura, "Liquid-Phase Epitaxial Growth of InGaAsSb/GaSb and InGaAsSb/AlGaAsSb DH Wafers," Japanese J. Appl. Phys., 18, 2169 (1979).
67. N. Kobayashi and Y. Horikoshi, "DH Lasers Fabricated by New III-V Semiconductor Material InAsPSb," Japanese J. Appl. Phys., 19, L641 (1980).
68. N. P. Esina, N. V. Zotova, B. A. Matveev, N. M. Stus', G. N. Talalakin and T. D. Abishev, "Long Wavelength Uncooled Light Emitting Diodes from  $\text{InAs}_{1-x-y}\text{Sb}_x\text{P}_y$  Solid Solution," Soviet Tech., Phys. Lett., 9, 4, 167 (1983).
69. E. R. Gertner, D. T. Cheung, A. M. Andrews and J. T. Longe, "Liquid Phase Epitaxial Growth of  $\text{InAs}_x\text{Sb}_y\text{P}_{1-x-y}$  Laser on InAs," J. Electronic Mat., 6, 163 (1977).
70. C. J. Nuese and G. H. Olsen, "Room Temperature Heterojunction Laser Diodes of  $\text{In}_x\text{Ga}_{1-x}\text{As}/\text{In}_y\text{Ga}_{1-y}\text{P}$  with Emission Wavelength between 0.9 and 1.15  $\mu$ m," Appl. Phys. Lett., 26, 528 (1975).
71. C. J. Nuese, G. H. Olsen, M. Ettenberg, J. J. Gannon and T. J. Zamerowski, "CW Room Temperature  $\text{In}_x\text{Ga}_{1-x}\text{As}/\text{In}_y\text{Ga}_{1-y}\text{P}$  1.06  $\mu$ m Lasers," Appl. Phys. Lett., 29, 807 (1976).

72. R. E. Nahory, M. A. Pollack, E. D. Beede, J. C. DeWinter and R. W. Dixon, "Continuous Operation of 1.0- $\mu$ m-Wavelength  $\text{GaAs}_{1-x}\text{Sb}_x/\text{Al}_y\text{Ga}_{1-y}\text{As}_{1-x}\text{Sb}_x$  Double Heterostructure Injection Lasers at Room Temperature," *Appl. Phys. Lett.*, 28, 19 (1976).
73. R. E. Nahory and M. A. Pollack, "Low-Threshold Room Temperature-Double Heterostructure  $\text{GaAs}_{1-x}\text{Sb}_x/\text{Al}_y\text{Ga}_{1-y}\text{As}_{1-x}\text{Sb}_x$  Injection Lasers at 1- $\mu$ m Wavelengths," *Appl. Phys. Lett.*, 27, 562 (1975).
74. H. Tamkin, K. Alavi, W. R. Wagner, T. P. Pearsall and A. Y. Cho, "1.5-1.6  $\mu$ m  $\text{Ga}_{0.47}\text{In}_{0.53}\text{As}/\text{Al}_{0.98}\text{In}_{0.52}\text{As}$  Multiquantum Wall Lasers Grown by MBE," *Appl. Phys. Lett.*, 42, 845 (1983).
75. A. F. S. Penna, J. Sah, A. Pinczuk, D. Sivco and A. Y. Cho, "Optical Investigation of Modulation-Doped  $\text{In}_{0.53}\text{Ga}_{0.47}\text{As}/\text{In}_{0.48}\text{Al}_{0.52}\text{As}$  Multiple Quantum Well Heterostructures," *Appl. Phys. Letts.*, 46, 184 (1985).
76. H. Ando, H. Kanbe, T. Kimura, T. Yamaoka and T. Kaneda, "Characteristics of Germanium Avalanche Photodiodes in Wavelength Region of 1-1.6  $\mu$ m," *IEEE J. Quantum Electron*, QE-14, 804 (1978).
77. C. A. Burrus, A. G. Dentai and T. P. Lee, "InGaAsP p-i-n Photodiodes with Low Dark Current and Small Capacitance," *Electron. Lett.*, 15, 655 (1979).
78. T. Takanashi and Y. Horikoshi, "InGaAsP/InP Avalanche Photodiode," *Japan J. Appl. Phys.*, 17, 2065 (1978).
79. K. Ogawa and E. L. Chinnock, "GaAs FET Transimpedance Front-end Design for a Wideband Optical Receiver," *Electron. Lett.*, 15, 650 (1979).
80. A. G. Thomson and J. C. Woolley, "Energy-Gap Variation in Mixed III-V Semiconductor Alloys," *Can. J. Phys.*, 45, 255 (1967).
81. J. W. Harrison and J. R. Hanser, "Theoretical Calculations of Electron Mobility in Ternary III-V Compounds," *J. Appl. Phys.*, 47, 292 (1978).

APPENDIX A. THEORETICAL BACKGROUND OF THE EQUATIONS  
PUBLISHED BY A. SASAKI ET AL. [25]

There are two types of quaternary mixed semiconductors composed of groups III and V elements:  $A_{1-x}^{III}B_x^{III}C_{1-y}^{V}D_y^{V}$  and  $A_{x-x-y}^{III}B_{x-x-y}^{V}C_{1-x-y}^{V}$  or  $A_{x-y}^{V}B_{x-y}^{V}C_{1-x-y}^{III}D_{1-x-y}^{III}$ . Here, the superscripts III and V indicate the group number of the atomic elements in the periodic table.

According to the formula proposed by Thompson and Wooley [80], the energy-gap variation of the  $A_{1-x}^{III}B_x^{III}C_{1-y}^{V}D_y^{V}$  type of mixed semiconductor can be calculated from

$$E_{ABCD} = E_{ABD}y + E_{ABC}(1-y) - \frac{\alpha_{ABCD}}{\sqrt{(E_{ABD} + E_{ABC})/2}} y(1-y) ,$$

where

$$E_{ABC} = E_{BC}x + E_{AC}(1-x) - \frac{\alpha_{ABC}}{\sqrt{(E_{BC} + E_{AC})/2}} x(1-x) ,$$

$$E_{ABD} = E_{BD}x + E_{AD}(1-x) - \frac{\alpha_{ABD}}{\sqrt{(E_{BD} + E_{AD})/2}} x(1-x) ,$$

and

$$\alpha_{ABCD} = \alpha_{BCD}x + \alpha_{ACD}(1-x) .$$

Here,  $E$  is the energy gap and  $\alpha$  is a parameter, called the "energy gap sag," representing the deviation of the energy gap curve from the linear dependence at the middle of the composition as a function of the composition  $x$  and  $y$ , at which the deviation becomes maximum. The subscripts AB, ABC, and ABCD denote the binary, ternary, and quaternary mixed semiconductors, respectively.

The energy-gap variations of the  $AB_{x-y}^{III}C_{1-x-y}^{V}$  type of material can be calculated from

$$E_{ABCD} = \frac{1}{x+y} (E_{ABD}x + E_{ACD}y) - \frac{\alpha_{ABC}}{\sqrt{(E_{ABD} + E_{ACD})/2}} x \cdot y ,$$

$$E_{ABD} = E_{AB}(x + y) + E_{AD}(1 - x - y) - \frac{\alpha_{ABD}}{\sqrt{(E_{AB} + E_{AD})/2}} (x+y)(1-x-y) ,$$

and

$$E_{ACD} = E_{AC}(x + y) + E_{AD}(1 - x - y) - \frac{\alpha_{ACD}}{\sqrt{(E_{AC} + E_{AD})/2}} (x+y)(1-x-y) .$$

The values of parameter  $\alpha$  were taken mostly from experimental data and are tabulated in Ref. 25. For unknown parameters, which are X valley for InGaP and  $\Gamma$  and X valleys for GaAsP, 0.3 was used as proposed by Thomson and Wooley [80].

It was assumed that the variation of lattice constant with composition follows Vegard's law, which shows linear dependence on the compositions. Thus,

$$a_{ABCD} = (1-x)(1-y)a_{AC} + x(1-y)a_{BC} + (1-x)y a_{AD} + xy a_{BD}$$

for  $A_{1-x}B_xC_{1-y}D_y$  type, and

$$a_{ABCD} = x a_{AB} + y a_{AC} + (1-x-y)a_{AD}$$

for  $AB_xC_yD_{1-x-y}$  type. In Fig. 3 only equal lattice constant lines equal to that of a binary compound are shown.

The refractive index  $n$  near wavelength  $1 \mu m$  is given by  $n \approx \sqrt{\epsilon_r}$  where  $\epsilon_r$  is relative dielectric constant. The variations of the relative dielectric constant with composition have not been theoretically investigated yet.

Therefore, the formulae adopted for ternary material by Harrison and Hanser [81] were applied to quaternary materials.

$$\begin{aligned} \frac{\epsilon_{r ABCD} - 1}{\epsilon_{r ABCD} + 2} &= (1-x)(1-y) \frac{\epsilon_{r AC} - 1}{\epsilon_{r AC} + 2} + (1-x)y \frac{\epsilon_{r AD} - 1}{\epsilon_{r AD} + 2} \\ &+ x(1-y) \frac{\epsilon_{r BC} - 1}{\epsilon_{r BC} + 2} + xy \frac{\epsilon_{r BD} - 1}{\epsilon_{r BD} + 2} \end{aligned}$$

for the  $A_{1-x}B_xC_{1-y}D_y$  type, and

$$\frac{\epsilon_{r ABCD} - 1}{\epsilon_{r ABCD} + 2} = x \frac{\epsilon_{r AD} - 1}{\epsilon_{r AB} + 2} + y \frac{\epsilon_{r AC} - 1}{\epsilon_{r AC} + 2} + (1-x-y) \frac{\epsilon_{r AD} - 1}{\epsilon_{r AD} + 2}$$

for the  $AB_xC_yD_{1-x-y}$  type.

END

4-87

DTIC